THESIS

CAVITY ENHANCED INSTRUMENTS FOR DETECTION OF HYDROGEN CHLORIDE AND AEROSOL OPTICAL EXTINCTION

Submitted by

Isaiah S. Franka

Department of Mechanical Engineering

In partial fulfillment of the requirements

For the Degree of Master of Science

Colorado State University

Fort Collins, Colorado

Spring 2013

Master's Committee:

Advisor: Azer P. Yalin

Sonia M. Kreidenweis
Anthony J. Marchese

ABSTRACT

CAVITY ENHANCED INSTRUMENTS FOR DETECTION OF HYDROGEN CHLORIDE AND AEROSOL OPTICAL EXTINCTION

This thesis concerns the development of cavity enhanced instruments for atmospheric science studies. Hydrochloric acid (HCl) is an important reservoir species for active halogens which are thought to participate in cycles that deplete ozone. In order to understand these halogens and their effect on ozone depletion, a cavity ring-down spectroscopy (CRDS) based instrument was developed for ultra-sensitive HCl concentration measurements. The instrument has a (1σ) limit of detection of 10 pptv in 5 min and has high specificity to HCl. Aerosols are a fundamental contribution to Earth's radiation budget and represent one of the largest unconstrained unknowns in estimating climate change. The effect of aerosols on climate and air quality is closely tied to their spectral properties as well as particle chemical composition, size, and shape. Aerosol extinction coefficient (sum of light attenuation by scattering and absorption coefficients) is an important optical property for determining aerosol radiative forcing. A broadband cavity enhanced absorption spectroscopy (CEAS) laser-based instrument for measurement of aerosol extinction has been created with a minimum detectable extinction coefficient of 8×10^{-8} cm^{-1} for 10-ms collection time. This thesis details the development and validation of these cavity enhanced spectroscopy based instruments.

ACKNOWLEDGMENTS

I would like to thank numerous people who supported the creation of this thesis. The first is my advisor Dr. Azer Yalin who guided my efforts for the last three years. I would also like to thank my lab mentor Brian Lee for his countless hours of hard work on the HCl CRDS instrument and his guidance in developing the aerosol CEAS instrument. Frank Loccisano, my other lab mentor, patiently and painstakingly taught me everything I know about physical optics. Without the patient support of my advisor and these mentors, this thesis would not have been possible. I would also like to thank fellow graduate students that I had the pleasure to work with over the course of my graduate school experience: Jordan Rath, Nick Wilvert, Randy Leach, Adam Friss, and many others. These individuals offered countless hours of support in my numerous research endeavors. Outside of the LPDL, I would like to thank Dr. Kevin Lehmann, Dr. Sonia Kreidenweis, Dr. Ezra Levin, and Dr. John Volckens for their guidance and help in the development of the aerosol CEAS sensor. Finally, I would like to thank my wonderful family for encouraging me daily.

TABLE OF CONTENTS

LIST OF FIGURES

1. INTRODUCTION

1.1 THE ROLES OF GREENHOUSE GASES AND AEROSOLS IN RADIATIVE FORCING

The atmosphere plays a significant role in the lives of all the inhabitants on planet earth. The atmosphere is responsible for controlling, protecting, regulating the Earth's surface by means of facilitating weather conditions, filtering harmful space radiation, determining temperature, etc. and ultimately makes life possible and sustainable. Within the numerous processes of the Earth's atmosphere, considerable effort has been made in recent years to study and better understand the effect of atmospheric species on radiative forcing. Radiative forcing (RF), as technically defined by the Intergovernmental Panel on Climate Change (IPCC), is "a measure of the influence a factor has in altering the balance of incoming and outgoing energy in the Earth-atmosphere system and is an index of the importance of the factor as a potential climate change mechanism" [1]. More simply put, this term refers to an externally imposed disturbance in the radiative energy budget of the Earth's climate system. These imbalances in the radiation budget (see Figure 1) have the potential to cause climate change and eventually could lead to a new equilibrium state of the climate system [2]. The various aforementioned climate discontinuities versus their respective radiative forcing values can be seen in Figure 1.

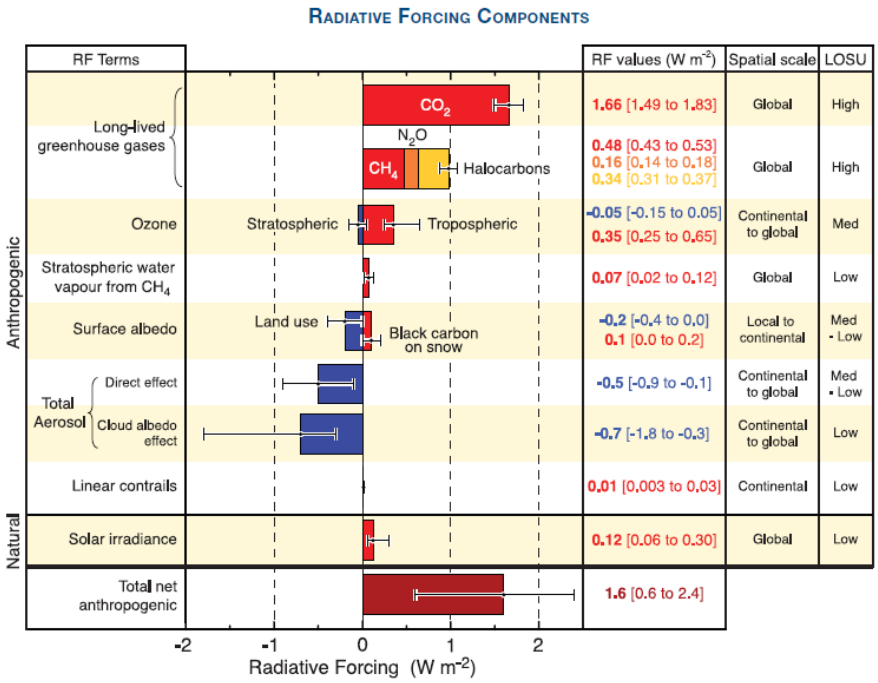

Figure 1 – The 2007 radiative forcings as estimated by the IPCC [1].

A positive forcing (more incoming energy) leads to a warmer system where as a negative forcing value (more outgoing energy) tends to cool the system down [1]. The concept of radiative forcing was first developed for one-dimensional radiative convective models and eventually led to subsequent models extrapolated to three dimensions. A simple linear relationship uses radiative forcing values to determine the change in global mean surface air temperature, ΔT [3]:

$$\Delta T = \lambda \Delta F \tag{1}$$

where λ is the model-dependent climate sensitivity parameter and ΔF is the global mean radiative forcing. Considerable strides have been made to understand how the changes in the atmospheric abundance of greenhouse gases and aerosols alter the Earth's energy balance. On an ongoing

basis, new observations and related modeling of greenhouse gases and aerosol are improving quantitative estimates of radiative forcing [1].

1.1.1 GREENHOUSE GASES

Greenhouse gases are a dominant source of radiative forcing contributions in the atmosphere. Numerous greenhouse gases occur naturally but increases in their atmospheric concentration over the last 250 years are largely a result of human activities. The effect of a greenhouse gas on the Earth's energy budget is determined by its transient concentration and its effectiveness at perturbing the radiative balance. Greenhouse gases can be divided into two major categories: long- and short-lived. Long-lived greenhouse gases (LLGHGs), such as Carbon Dioxide (CO_2), methane (CH_4), and nitrous oxide (N_2O), are chemically stable and remain in the atmosphere for tens to hundreds of years. Since these species are nearly temporally constant, they become well mixed throughout the atmosphere and reach an almost quasi-equilibrium concentration distribution. This constant distribution allows LLGHs concentration to be accurately estimated by measuring at a few locations across the globe. The other major subgroup, aptly named short-lived gases, is chemically reactive and generally removed from the atmosphere by washout in precipitation or by natural oxidation processes. Due to constant addition and removal of these gases from the atmosphere, they have a highly fluctuating concentration distribution. Ozone is a significant short-lived greenhouse gas that is formed and destroyed by chemical reactions involving other atmospheric species (discussed in greater detail below). In the troposphere, humans mainly affect ozone concentration by changing the precursor gases (e.g. HCl) that ultimately lead to ozone creation. In the stratosphere, human influence has been on ozone-depleting substances, which as their name suggest, affect ozone

removal rate. As can be seen in Figure 1, ozone makes a considerable contribution to the Earth's energy budget in which it has a positive radiative forcing value in the troposphere and a negative value in the stratosphere [1].

1.1.2 AEROSOL CONTRIBUTIONS

As can be concluded from an uncertainty analysis ("error-bars" in Figure 1), the effects of long-lived greenhouse gases on earth's radiative energy balance is relatively well understood and accurately measured. Conversely, the uncertainty associated with aerosol radiative forcing is significantly large and is indicative of the limited physical understanding of how aerosols interact with the atmosphere. Since aerosols play a major role in the radiative energy balance, their forcing uncertainty leads to obvious uncertainty in climate change predictions. It has been proposed that radiative forcing effects of sulfate-containing aerosols could be equal in magnitude to, and opposite in sign to, the radiative forcing induced by greenhouse gases [4]. For this reason there is a strong need to understand the role that aerosols play on the radiation balance of the atmosphere.

Although an aerosol is defined as any mixture of particles and gas phase diluents, the focus is placed on the particles and, therefore, the term aerosol refers to these particles. There are various natural and anthropogenic sources from which an aerosol can be created (see Figure 2). Primary aerosols are produced directly at the source whereas secondary aerosols are mostly formed from gaseous precursors by numerous gas and aqueous phase oxidation pathways. Examples of primary aerosols are fly ash of industrial origins, sea-salt particles coming off the ocean surface, or minerals which are a result of wind across an arid landscape.

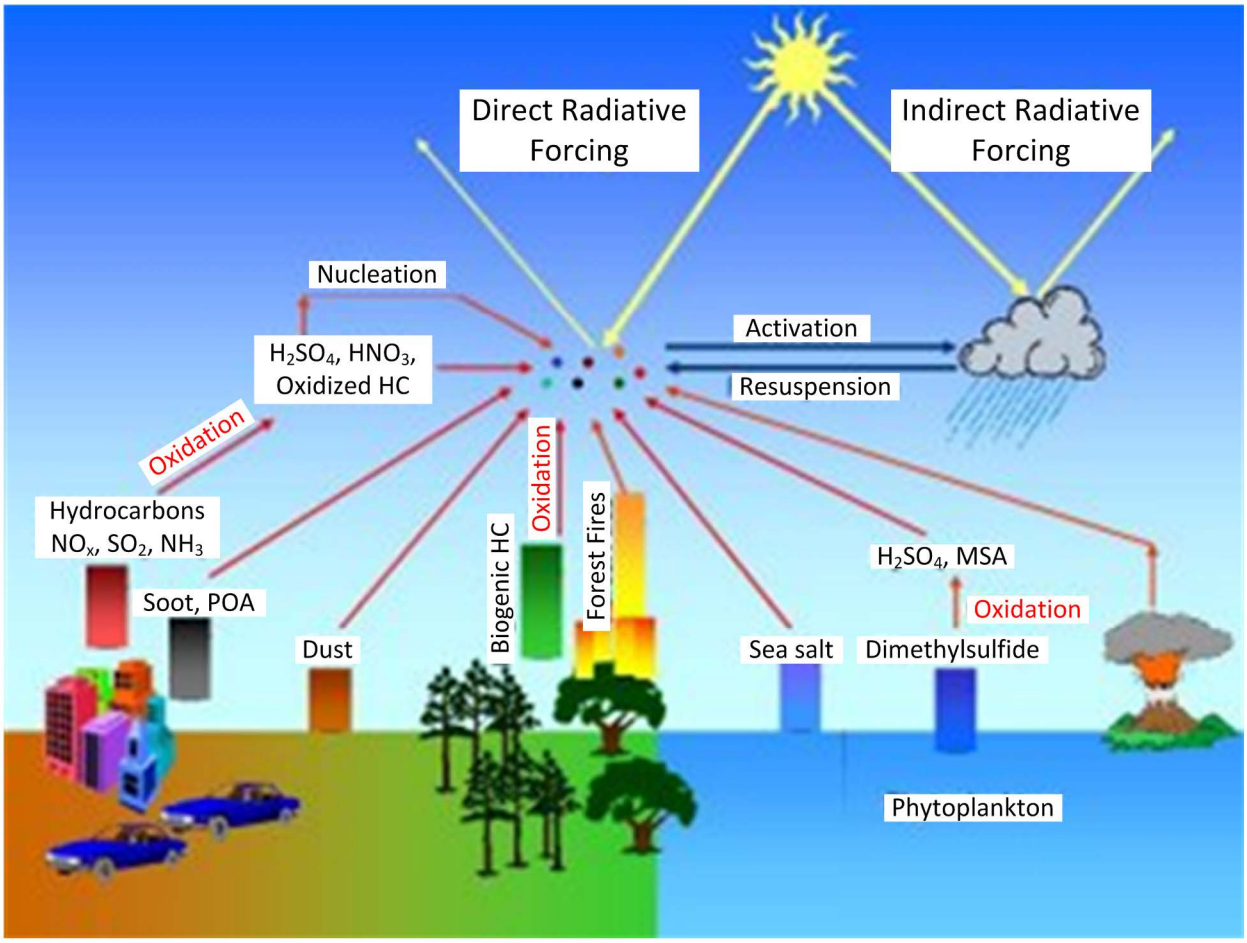

Figure 2 - Natural and anthropogenic sources of aerosols [5].

An example of secondary aerosols is provided by sulphate particles which can be created by dimethyl sulphide emissions of phytoplankton and/or sulphur emissions from the burning of fossil fuels. The result of so many geographically localized sources leads to aerosol distribution being spatially inhomogeneous [3].

Once aerosols are created, they undergo complicated chemical reactions in the Earth's atmosphere, mixing and reacting with other aerosols or themselves. Finally, aerosols can leave the atmosphere by either colliding with the Earth's surface or raining out in a cloud. The length of time between aerosol creation and deposition can range anywhere from a few minutes to

several weeks which ultimately creates a fluctuating temporal distribution of aerosols in the atmosphere [3]. Aerosols are a form of direct radiative forcing because they scatter and absorb radiation in the atmosphere (discussed in more detail later). Aerosols can also modify the creation and precipitation efficiency of liquid water, ice and mixed-phase clouds, thus causing indirect radiative forcing related to these cloud property changes. Quantifying the radiative forcing of aerosols is difficult because aerosol mass and particle number concentrations are highly unpredictable in space and time; this variability is mostly due to aforementioned shorter atmospheric lifetime of aerosols compared to other atmospheric species (greenhouse gas, etc.) [6].

There is, therefore, a high demand for spatially and temporally resolved data of the atmospheric burden and radiative properties of aerosols since these parameters are needed for calculating radiative forcing. Satellite observations, as seen in [7], provide a means of determining regional variations in aerosols; however, they are expensive and quite rare. Therefore, models must be implemented in order to interpolate and extrapolate the available data in hopes of determining accurate aerosol radiative forcing values and climate change predictions. Despite the large uncertainties related to their implementation, models are the primary method for studying past or future aerosol properties and distributions [6].

1.2 TROPOSPHERIC HYDROGEN CHLORIDE

Chemical reactions involving halogen radical species, such as chlorine and bromine atoms and their oxides, significantly influence the composition of the earth's atmosphere. These species also play important roles in many atmospheric processes such as those that determine precipitation acidity and the formation and destruction of ozone. In remote regions of the

troposphere, such as the polar boundary layer, these species are thought to contribute to destruction of ozone [8], [9]. The ozone depletion, along with formation of new oxidizing agents, may ultimately lead to a change in the dominant oxidizing agents. In contrast, in marine boundary layers in populated coastal regions, the halogen species can contribute to ozone formation [10], [11]. Other atmospheric processes in the marine boundary layer, such as the oxidation of methane [12], [13] and larger hydrocarbons [14], can also be influenced by these species. The radical chlorine species also play a key role in ozone destruction within the upper stratosphere [15].

Hydrochloric acid, HCl, is an important reservoir species for active halogens. Studies of composite chlorine emissions indicate that HCl is the dominant gas-phase contributor to the overall chlorine inventory in the lower atmosphere [16], [17]. The principal source of HCl in the lower atmosphere (marine boundary layer) is thought to be from sea-spray generation, though the extent of the contribution from anthropogenic activity such as coal burning is not well understood. Chlorine present in the sea-salt aerosols generated by wind stress at the ocean surface is converted to HCl by acid-displacement reactions [18], [19]. Typical HCl concentrations in remote marine environments span from tens to hundreds of parts per trillion [20], while reaching levels of several parts per billion in coastal urban areas [18], [21]. In the upper atmosphere (>~40 km), HCl is thought to account for more than 90% of the total chlorine [15]. However, estimates of HCl production vary considerably and existing measurements are limited. As is further discussed below, there remains a strong need for improved measurement techniques for HCl, as is addressed in the present contribution. From an industrial perspective, high-temperature chlorine corrosion via HCl can be a costly problem for combustion and gasification plants [22], [23], which provides additional motivation for developing HCl sensors.

1.2.1 METHODS FOR HCL DETECTION

The understanding of sources and sinks of HCl, as well as the role of HCl in proposed chemical mechanisms, requires suitable measurement techniques with sufficient accuracy, sensitivity, and time-response. Currently, the available instruments for such studies are rather limited. The original method for such studies was to sample gas phase HCl into a solution using a mist chamber collector, and to analyze the solution by high resolution ion chromatography (e.g., [24], [25]). The method is attractive owing to its relative simplicity and reliability, but limitations include relatively slow time resolution (typically 10s of minutes or more) and potential specificity issues. Although the measured signal is primarily due to HCl, the measurement can be influenced by contributions from other active chlorine species, such as $ClNO_2$, so that the measurement is often referred to as HCl* [18], [24].

Another method for HCl detection is to use chemical ionization mass spectrometry (CIMS) [20], [26], [27]. The CIMS instruments allow selective, rapid and sensitive detection species detection and are amenable to both ground based and aircraft deployments [28]. A potential limitation of these techniques is their specificity which depends on the details of the ion chemistry scheme; for example, Marcy *et al.* have reported sensitivity to water vapor [29]. From a practical point of view, the CIMS systems tend to require relatively extensive inlet and transfer lines, which can be problematic for sticky gases like HCl [26]. The CIMS systems also require periodic calibrations, while the need for a sensitive mass spectrometer significantly increases the cost of the technique as compared to optical approaches.

Optical absorption based measurements of HCl using infrared laser sources are also possible. By selecting an absorption line of the target species, i.e. $H^{35}Cl$, which does not have nearby interferences from other atmospheric constituents, the optical measurements can be

highly species specific. Past work has employed tunable diode lasers in a multi-pass Herriot cell for HCl detection [30], [31]. The system was sensitive, species-specific, allowed rapid-time response (see Section 2.2.2 – where time response is discussed) and was amenable to airborne deployment. In order to access the strongest fundamental vibrational band, the system employed lead salt lasers at 3.4 μm paired with mercury-cadmium-telluride (MCT) detectors, both of which required liquid nitrogen (LN_2) cooling.

1.3 OPTICAL PROPERTIES OF ATMOSPHERIC AEROSOLS

The optical properties of aerosols are responsible for numerous remarkable atmospheric phenomena such as vibrant sunsets and rainbows. Aerosols also cause visibility degradation associated with atmospheric pollution [32]. Furthermore, there exists a link between climate change and aerosol optical properties. The radiative properties of atmospheric aerosols depend on aerosol size distribution and composition. However, in order to calculate the RF of a given aerosol (and associated uncertainty), various optical properties are necessary. These properties can be condensed into a small set of four quantities which are a function of wavelength: the mass light-scattering efficiency, the functional dependence of light-scattering on relative humidity, the asymmetry parameter, and finally the single-scattering albedo (SSA) [6]. The emphasis of this thesis is on the measurement of SSA, more specifically its extinction component, which will be discussed for the remainder of this section.

Owing to the large size compared to molecules, aerosols significantly scatter and/or absorb incident radiation. Aerosols that primarily scatter exert a net negative direct RF (cools the earth) whereas partially absorbing aerosol may exert negative RF over dark surfaces (e.g.

oceans, forests, etc.) and positive RF (warms the earth) over light surfaces (e.g. desert, snow, etc.) [2]. Since optical extinction coefficient (sum of scattering and absorption coefficients [33]) is specific to particulate size and composition, aerosols create temperature gradients in the atmosphere. Single-scattering albedo (SSA) (parameter that simplifies aerosol extinction) is technically defined as the ratio of scattering coefficient to total extinction coefficient [34]. (Note, the terms extinction and extinction coefficient will be used interchangeably). The direct radiative effect of aerosols is also very sensitive to the small changes in SSA (e.g. a change in SSA from 0.9 to 0.8 can frequently change the sign of the direct effect as seen in [35];[6]). For spherical particles, it is common to use Mie Theory in conjunction with material optical properties to calculate the SSA [36]. Conversely, discrete two-stream approximations are implemented in order to determine the SSA of non-spherical particles [37]. The Mie solution of SSA, although exact, has limited utility since various wavelength-dependent optical properties are needed (index of refraction, scattering angle, size parameter, etc.) and therefore, direct measurement is preferable.

1.3.1 MEASUREMENT TECHNIQUES

Determination of SSA requires measurement of two out of three of absorption, scattering, and extinction coefficients, for example, measurement of absorption and extinction separately [6]. The scattering properties are generally measured by a number of techniques such as nephelometry, lidar, and passive spectroradiometry of the solar radiation. The measurement of absolute optical extinction, or alternatively the transmission, is still a considerable measurement challenge since Rayleigh equivalent (molecular scattering) losses are extremely low for clear air and can be more than four orders of magnitude larger for polluted air [38]. Aerosol light

absorption generally cannot be measured accurately and, therefore, is determined by subtracting the measured scattering from the optical extinction; very careful calibrations are required because the absorption is often a difference between two large values. There are, however, a few cases where aerosol light absorption is actually measured directly. An example of this is the use of photo-acoustic spectroscopy in conjunction with a filter technique to measure absorption values [6], [39]. However, these results also pointed to strong wavelength dependence in the light absorption and rendered such results only moderately useful. Other than this synthesis method, the other techniques commonly used for determining SSA are extinction cell, filter techniques, irradiance measurements, and black carbon mass by thermal evolution. Airborne comparisons of these techniques were made [6], [40] in biomass burning plumes and hazes. It was found that measured regional averages of SSA were within about 0.02 for all techniques except thermal evolution, however, individual data points were only slightly correlated with regression coefficient values of about 0.6. SSA is difficult to retrieve from satellites, especially over oceans as determined in [6], [7], [41]. This issue is related to satellites' viewing geometry, which limits measurements to light scattering rather than extinction for most tropospheric aerosols. Accurate values of SSA can be determined from satellite data for some specific conditions, especially when coupled with ground measurements [6], [42], [43].

1.4 CAVITY ENHANCED MEASUREMENT TECHNIQUES

In order to accurately measure various properties of atmospheric species, cavity enhanced measurement techniques are commonly implemented (briefly discussed in 1.2.1 and 1.3.1). Cavity enhanced spectroscopy is generally characterized by the use of high finesse optical

cavities, which greatly increase the effective path length of interaction between an incident laser and sample. The sample (e.g. gas or aerosol) is housed within the cavity and a detector at the cavity output measures the light extinction due to the sample, which can ultimately be related to various properties. In this thesis, two variations of this method, Cavity Ring-Down Spectroscopy (CRDS) and Cavity Enhanced Absorption Spectroscopy (CEAS) have been implemented to measure HCl concentration and aerosol extinction, respectively. These are further discussed in the following subsections.

1.4.1 CAVITY RINGDOWN SPECTROSCOPY (CRDS)

Cavity ring-down spectroscopy (CRDS) is an ultra-sensitive laser-based absorption technique that may be used to measure trace species in the gas phase [44], [45]. The technique is seeing growing use in a range of fields including combustion diagnostics, plasma diagnostics, basic spectroscopy studies, and atmospheric trace gas detection. In addition to its sensitivity, the principal advantages for the use of CRDS in the atmosphere include selectivity, which comes from spectral discrimination, directly quantitative detection of trace species based on known absorption cross sections, and the possibility of versatile sensor hardware (small, lightweight, low power consumption) for field use.

The sensitivity of CRDS is achieved by measuring optical extinction due to the gas sample (in this case atmospheric air containing HCl) within a high-finesse optical cavity. As shown in Figure 3, the optical cavity is typically formed from two (or three) high-reflectivity mirrors.

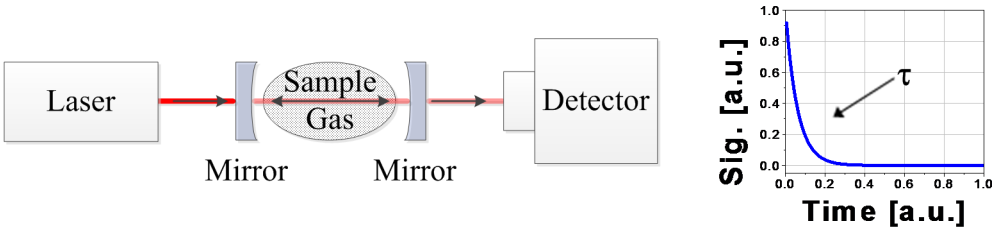

Figure 3 - Schematic diagram of CRDS setup. Laser light makes multiple (>10^4) passes within cavity. The decay rate of the cavity light intensity is measured and provides absorber concentration.

The interrogating laser beam is coupled into the optical cavity where it makes multiple passes between the mirrors. In many spectral regions, mirrors with reflectivity >0.9999 are available, so that the light makes more than 10^4 passes within the cavity. The effective path length is therefore greatly increased relative to single-pass absorption (or even typical multi-pass Herriot cell measurements). A detector behind the cavity measures the temporal decay (ring-down) of the light intensity in the cavity. When the laser is resonant with the absorbing sample (e.g. HCl), there is stronger (faster) decay. The difference between the decay-rate with the absorbing sample, and without the absorbing sample, gives a measure of the sample concentration. A conversion of decay-rate into concentration will be given in a subsequent section.

1.4.2 CAVITY ENHANCED ABSORPTION SPECTROSCOPY (CEAS)

An alternative to CRDS is to determine the time averaged power transmission of the optical cavity, instead of its decay rate, and this method is known by both the names Cavity Enhanced Absorption Spectroscopy (CEAS) [46] and Integrated Cavity Output Spectroscopy (ICOS) [47]. These techniques are also being increasingly used in atmospheric science [48–52]. As discussed in Section 1.3.1, these cavity enhanced methods (CRDS and CEAS) are now being

used to determine extinction from aerosols [33], [38], [53–69]. An attractive feature of these measurements is that they provide an absolute measurement of loss and do not require determination of calibration factor, such as collection efficiency. Note that, following the literature, the term CEAS for extinction measurement will sometimes be used, however, the technique really provides total loss, i.e. extinction. (The term "absorption" is often used since in gas-phase spectroscopy, where there is relatively weak scattering, absorption spectra are measured.)

Much like CRDS, typical implementations of CEAS have used narrow bandwidth lasers for cavity excitation with spectra obtained by scanning these lasers. There have also been some reports of "broad bandwidth" configurations that have used spectrally broad sources to excite the cavity and then disperse the different frequency components of the light transmitted through the cavity, typically using either a grating [70–75] or Fourier Transform spectrometer [76–78]. However, in almost all of this previous work the "broad bandwidth" that could be simultaneously covered by one instrument was limited to a fractional bandwidth of a few percent or less by the high reflectivity bandwidth of the low loss dielectric mirrors that have been used to construct the cavity. Dielectric mirrors achieve their high reflectivity, R, by constructive interference of the modest Fresnel reflection from a large number of interfaces between alternatively high and low index materials, separated by $\lambda/4$. An alternative is to use instead Prism retroreflectors to form the cavity, as shown in Figure 4 [79], [80].

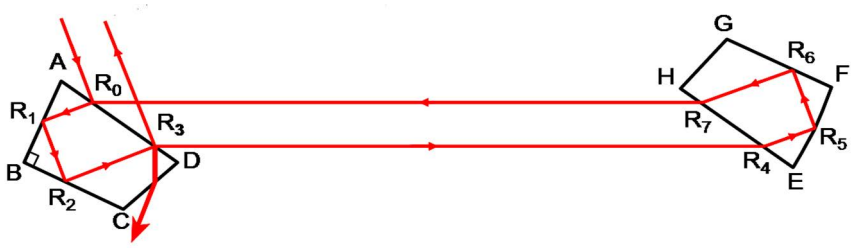

Figure 4 - Brewster's angle retroreflector based optical cavity [79–82]

The cavity is formed from two prisms. Light enters and exits each prism (R_0, R_3, R_4, R_7) at very near Brewster's angle and thus P polarized light (polarization vector in the plane of the page) experiences very low reflective loss. Brewster's angle, θ_B, is determined by $\tan(\theta_B) = n$, where n is the index of refraction of the prism material (and the surrounding air is treated as free-space with unity index-of-refraction). Within each prism, light undergoes two total internal reflections (R_1, R_2, R_5, R_6) and returns antiparallel to the input ray. With a pair of such prisms, aligned relative to one another as in Figure 4, one forms a ring cavity. One optic surface (e.g. EF in Figure 4) has spherical shape to provide focusing as needed for a stable cavity. Light is coupled into and out of the cavity (A and C) by tilting the input/output prism slightly away from Brewster's angle.

In order to utilize the prism cavities for simultaneous broad bandwidth detection, one must use a spectral light source that covers the full spectral range one is interested in. In addition, high brightness is desired, since the transmission of a high-finesse cavity is quite low for continuum light, and high spatial coherence, since one wants to maximize coupling into the TEM_{00} mode of the cavity. Some groups have used mirror based cavities with incoherent light sources such as discharge lamps or light emitting diodes, but a much higher brightness source is available, a supercontinuum generated by pumping a photonic crystal (PC) fiber [83–85]. With

such a fiber, ~50% of the light power can be converted from a narrow bandwidth laser, such as Nd:YAG, into a spectrally broad continuum covering a range from ~400-1800 nm [86]. Further, since the continuum light is emitted from the core of the fiber (which is only ~4 μm in diameter), it is highly spatially coherent, unlike radiation from lamps or LED's. Because of the strong non-linear interaction in the fiber core, only a few kW of peak power is required to generate the supercontinuum. The Lehmann group was the first to use such a supercontinuum light source for cavity enhanced spectroscopy and initial results were published in Optics Express [82]. Eq. 2 shows how the absolute extinction strength of a sample inside the cavity, $\alpha(\nu)$, versus light frequency, ν, can be calculated from the measured spectra of light transmitted:

$$\alpha(\nu) = \left(c\tau(\nu)\right)^{-1}\left(1 + n\frac{L_p}{L_g}\right)\left(\frac{I^0(\nu)}{I(\nu)} - 1\right), \tag{2}$$

where $I(\nu)$ is the intensity transmitted by the cavity with sample, $I^0(\nu)$ is the intensity transmitted by the empty cavity, c is the speed of light, $\tau(\nu)$ is the empty cavity photon lifetime (ring-down time), n the index of refraction of the prisms, L_p the single pass path length inside a prism, and L_g the path length in the gas. The factor $(1 + n\, L_p/L_g)$ corrects for the fraction of time the photons spend in the sample.

Figure 5 shows a schematic of the instrument that Lehmann *et al.* used for doing broad-bandwidth CEAS with SiO_2 prisms. In this experiment, the cavity decay time was 33 μs, for which the factor $(c\ \tau(\nu))^{-1} = 1\text{x}10^{-6}$ cm^{-1}.

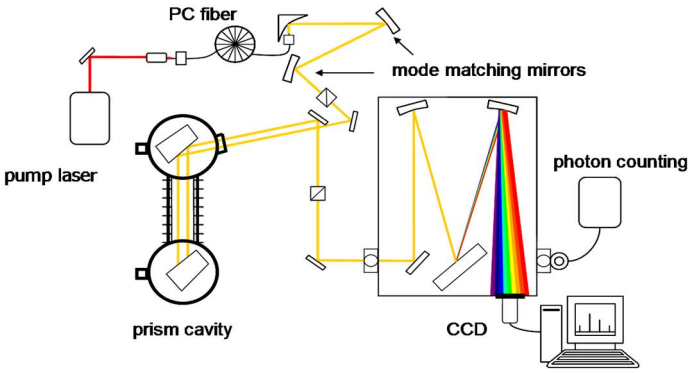

Figure 5 - Schematic of the ultra-broadband cavity enhanced absorption spectrometer.

The sensitivity of the instrument is determined by this factor times the noise in determination of the ratio of $I(\nu)/I^0(\nu)$. Figure 6 shows an example spectrum obtained with this instrument, the electronic band of O_2 near 695 nm, observed in ambient air.

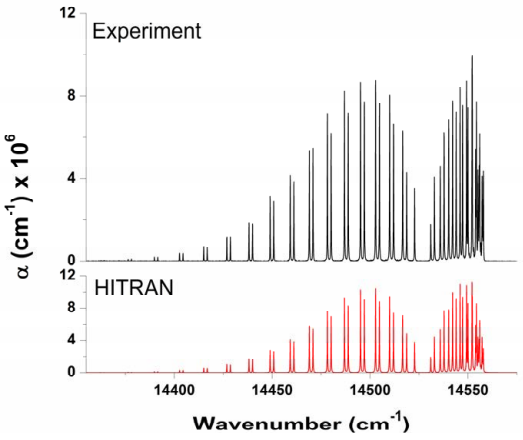

Figure 6 - The experimental CEAS of the b $^1\Sigma_g^+$-X $^3\Sigma_g^-$ (v = 1 ← 0) transition of molecular oxygen in air referenced to dry nitrogen gas, along with the HITRAN predicted spectrum.

1.5 PROBLEM STATEMENT AND THESIS LAYOUT

In the field of atmospheric science, there is a need for sensitive hydrogen chloride concentration measurements in order to understand its effect on various halogen chemistry and ozone depletion. Furthermore, there is a need to measure the extinction component of aerosol single-scattering albedo over various wavelengths for the purpose of determining radiative forcing. This thesis concerns the development of cavity enhanced instruments for these atmospheric science studies. In Chapter 2, a cavity ring-down spectrometer measuring HCl concentration will be presented. This chapter discusses the instrument description and performance (i.e. limit of detection, sensor verification, and field study demonstration). Chapter 3 will discuss the development of a cavity enhanced absorption spectrometer to the measure aerosol extinction. This section describes the optical setup and aerosol delivery systems implemented. Finally, chapter 4 concludes this thesis and offers future improvements for both sensors.

2. CAVITY RING-DOWN SPECTROSCOPY INSTRUMENT FOR DETECTION OF HYDROGEN CHLORIDE

A CRDS laser-based instrument for measurement of hydrogen chloride (HCl) has been developed and characterized. The instrument uses light from a distributed-feedback diode laser at 1742 nm coupled to a high finesse optical cavity to make sensitive and quantifiable concentration measurements of $H^{35}Cl$ based on optical absorption. The instrument has a (1σ) limit of detection of 10 pptv in 5 min and has high specificity to HCl. Validation studies with a previously calibrated permeation tube setup showed an accuracy of better than ~10%. The CRDS sensor was field tested in parallel with two other HCl measurement techniques (mist chamber and chemical ionization mass spectrometry), all of which were in good agreement. The instrument also allows sensitive measurements of water and methane and minimal hardware modification would allow detection of other near-infrared absorbers. The remainder of this chapter discusses the design, development, and validation of the HCl instrument.

2.1 INSTRUMENT DESCRIPTION

The specific design of a spectroscopic instrument for absorption measurements is guided by the location and strength of the targeted absorption feature. For this instrument, the R(3) $H^{35}Cl$ line of the (2-0) absorption band (see Figure 7 [87]) was chosen due to its relative strength, its separation from other atmospheric absorbers, and its accessibility using available near-infrared (NIR) components.

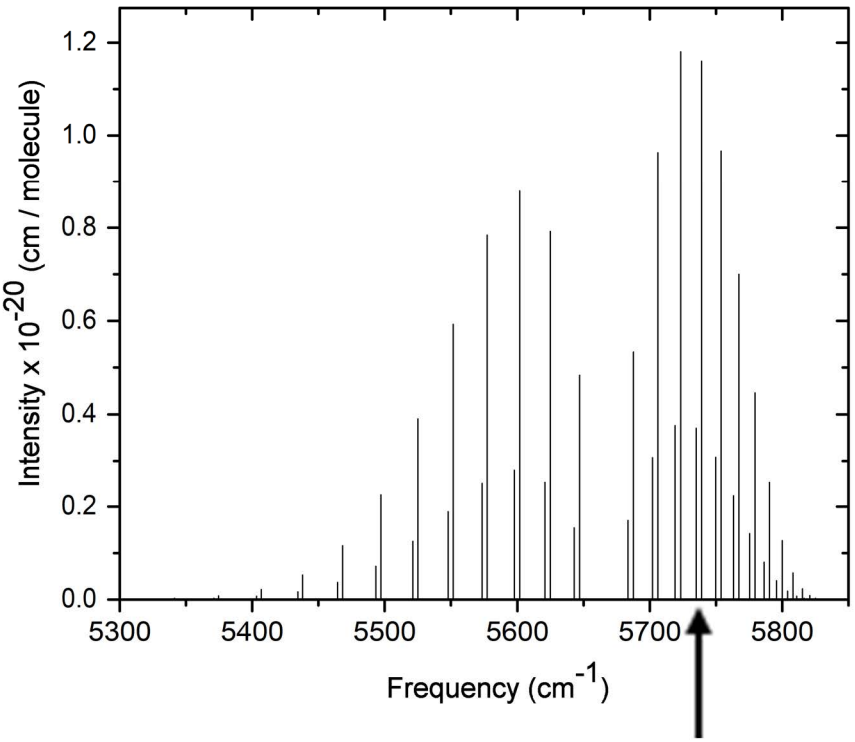

Figure 7 - Linestrengths of rotational lines of the 2-0 vibrational absorption band of $H^{35}Cl$ and $H^{37}Cl$ from HITRAN. The CRDS sensor uses the R(3) line of $H^{35}Cl$ at 5739.26 cm^{-1} as indicated by the arrow.

This line has also been selected by other researchers for laser absorption measurements of HCl [22], [88]. Although the selected wavelength of 1742 nm is slightly outside the standard telecommunications bands, nearly all of the needed equipment (laser, fiber optics, mirrors, etc) is available and applicable at this wavelength. The fundamental vibrational band of HCl near 3.4 μm has much stronger line strengths, however, the optical equipment needed for that wavelength region (e.g. difference-frequency generation laser sources [89]) is more expensive and less commercially developed.

Separation from the absorption lines of other potential interfering molecules is integral to successful measurements. Interference due to expected ambient molecules has been considered including: CH_4, CO, CO_2, HCl, H_2O, NO, and N_2O. As shown in Figure 8, the absorption spectra in the vicinity of the targeted HCl absorption line have been simulated.

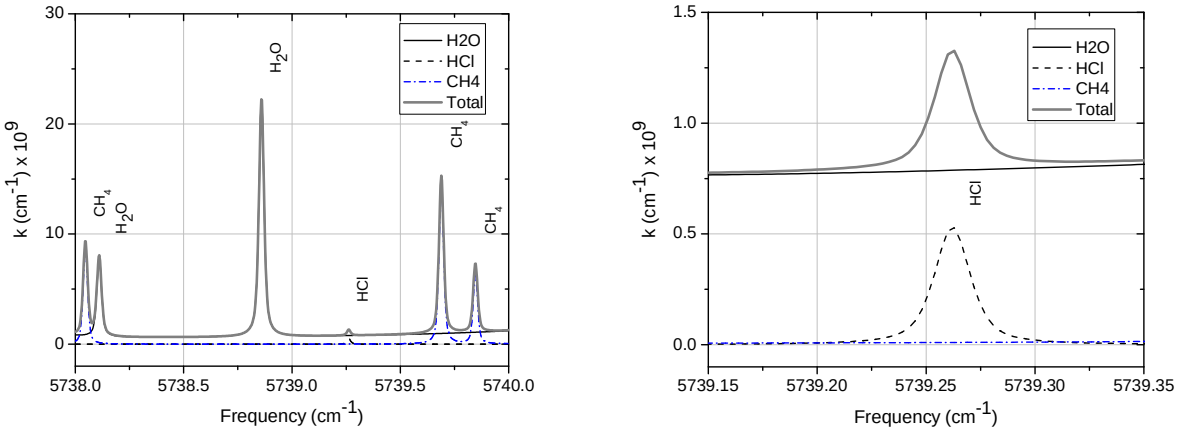

Figure 8 - Simulated absorption spectra in the vicinity of the targeted HCl absorption line. Simulated conditions are: P=0.1 bar, T=295 K, HCl=0.5 ppbv, CH_4=2 ppmv, H_2O=0.013 (50% Relative Humidity). Left/Right: Zoomed out/in of HCl line.

The simulations assume typical ambient species concentrations, spectral parameters from HITRAN, and standard expressions for thermal and collisional line broadening [87]. There is a tradeoff of operating pressure (i.e. the pressure in the ring-down cell where the optical measurement is performed) and possible performance at difference pressures have been examined which can be experimentally achieved by varying the flow cell and pumping conditions. Reducing the pressure tends to narrow the spectral absorption features and improve specificity, but at the cost of reduced signal amplitudes and, at sufficiently low pressure (<~0.05

bar), can introduce operational challenges with the flow system. An operating cell pressure of 0.1 bar was found to be a reasonable compromise in this regard.

The literature contains two slightly differing values for the line strength (cross-section) of the targeted HCl line (R(3) $H^{35}Cl$). The 2008 HITRAN database reports a linestrength of 1.16×10^{-20} cm/molecule for the R(3) $H^{35}Cl$ line, which is based on simulation [90]. More recently, Ortwein *et al.* experimentally studied the same line and reported it to be 1.25×10^{-20} cm/molecule [22]. For the instrument presented here, the experimental value from Ortwein *et al* is used.

Figure 9 shows the schematic layout of the CRDS system. The light source is a distributed-feedback diode laser (NEL Lasers, KELD1F5DAAA) in a 14-pin butterfly package with a center wavelength of 1742 nm, linewidth of a few MHz, and 13 mW of output power through a single-mode fiber pigtail. Light from the laser is first sent through a 99%-1% fiber-optic beam splitter.

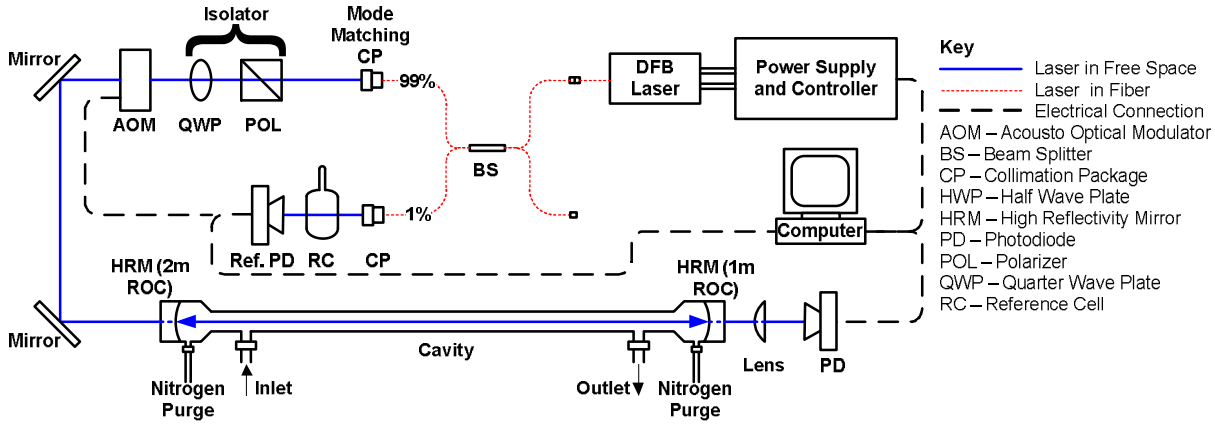

Figure 9 - Schematic of the optical components and data acquisition systems of the HCl sensor.

The 99% leg is used as the main interrogating beam, while the weaker leg is used for the frequency calibration leg. When the system is first run, the 1% output leg from the fiber splitter is sent through a low-finesse Fabry-Perot etalon (fused silica, 45 mm long, finesse ~20) and a photodiode (Thorlabs, PDA10CS) monitors the etalon transmission signal. The relative frequency of the laser (as determined by the etalon transmission peaks) is plotted against the voltage sent to the laser controller (ILX Lightwave, LDC-3714C) and fit to a second order polynomial, which then provides a relationship between (relative) laser frequency and controller voltage for subsequent use. This frequency determination procedure is done automatically in our custom LabVIEW software and takes only a few seconds. Owing to the high stability of the DFB laser, these fit coefficients proved stable over months. In regular operation, the etalon is replaced with a custom reference cell which is a sealed glass vessel containing a high concentration of HCl (~0.1%). As the instrument runs, the 1% leg of the beam splitter is sent through the reference cell, and the photodiode monitors the transmission. Due to the high concentration of HCl in the cell, a strong absorption feature is observed, even through a path length of only a few cm. The sensor control software finds the peak of this absorption feature and centers the laser scan on the HCl spectral feature, thus ensuring any ambient temperature changes do not cause the laser to drift away from the desired wavelength.

The 99% output leg from the fiber splitter is first sent through an aspheric collimation lens (Thorlabs, CFC-11X-C, f=11 mm). The aspheric lens is precisely positioned relative to the beam splitter in order to spatially mode match the beam to the $TEM_{0,0}$ mode of the cavity, which also requires proper separation of the cavity and lens [91]. After the collimation package, a polarizer and quarter-wave plate are used in series as an optical isolator, blocking reflected light from going back into the laser, which, even in small amounts, causes noticeable instability in the

laser. The last element before the high-finesse cavity is the acousto-optic modulator (AOM, IntraAction, ACM-402AA1). When the data acquisition (DAQ) system detects a resonance out of the optical cavity, the computer will turn off the AOM, causing the incoming laser to be rapidly extinguished (time constant of ~300 ns). The optical cavity itself is constructed of two high-reflectivity dielectric mirrors (Advanced Thin Films), with radii of curvature of 2 m and 1 m, and a separation of 90 cm. The mirror reflectivity, as determined from empty-cavity ring-down times of ~170 μs, is R=99.9982% (consistent with manufacturer specification).

Indium Gallium Arsenide (InGaAs) photodiodes are widely used for NIR detection, however, the responsivity of InGaAs diodes drops almost two orders of magnitude at 1742 nm as compared to the peak. Extended wavelength InGaAs diodes, with lower bandgap energies, provide higher responsivity farther into the IR, but the dark current also increases significantly. For detection of the main cavity beam, an extended wavelength InGaAs photodiode (Hamamatsu, G8421-03) soldered onto a transimpedance amplifier (Analog Modules, 341-4) is employed. The amplifier has an input capacitance matched to the photodiode, a gain adjusted to 2×10^6 V/A, and a bandwidth of 2 MHz. The bandwidth of 2 MHz is approximately 5 times larger than needed to not distort the ring-down signals, which results in increased noise, as high-frequency detector dark noise is unnecessarily amplified. Other detector options are discussed in 4.1. The cavity detector voltage signal is digitized by a 2.5 MS/s, 14-bit PCI multi-purpose DAQ card (National Instruments, PCI-6132), which also controls the AOM. A second DAQ card (National Instruments, PCIe-6321) is used to output the analog voltage signal to the laser controller, as well as to digitize the reference cell detector signal.

A custom LabVIEW program is used to control the instrument and to handle data acquisition and processing. First the software sends an analog voltage to the laser controller,

continuously scanning it from 5739.22 cm^{-1} to 5739.30 cm^{-1} and back. When the photodetector signal out of the cavity exceeds a pre-determined threshold (indicative of the laser being in resonance with the cavity), the LabVIEW software turns off the AOM, digitizes the ring-down signal, and fits the data to an exponential function using an iterative non-linear least squares fit seeded by a linear least-squares fit [80]. Whenever a ring-down event is recorded, the relative laser frequency is calculated from the previously discussed etalon calibration. The total DAQ system is capable of acquiring more than 200 ring-downs per second, which far exceeds what can be optically achieved (typically ~25 per second). Once the ring-down time is found, it is converted to an absorption coefficient, *k*, which still includes the empty-cavity loss, given by

$$k = \frac{1}{c\tau} \tag{3}$$

where c is the speed of light and τ is the ring-down time. The LabVIEW software collects ring-down signals for a set amount of time (typically 30 s), termed the integration time, after which the spectrum of recorded absorption values are fit to a Voigt profile, as shown in Figure 10. Curve fitting to a Voigt profile can be computationally expensive.

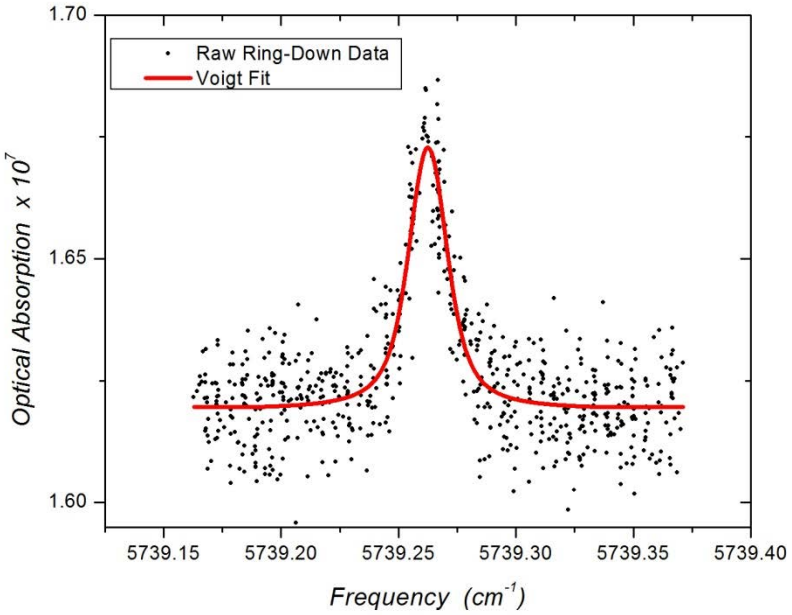

Figure 10 - Example plot of the measured dimensionless absorption values versus frequency in the vicinity of the HCl absorption feature after 30 seconds of acquisition time. The red line is a Voigt profile fit. The non-zero baseline is due to the cavity mirror loss. The measured HCl concentration in this case is 6.25 ppbv.

To avoid computer downtime, a table of pre-computed Voigt profiles is used [92]. In the current implementation, Voigt and Lorentzian spectral widths are calculated from the known gas conditions inside the sampling cell and used to look up the numerical Voigt profile from the table. The amplitude and offset of these numerical values are then scaled to achieve a linear least-squares fit to the data, and ultimately find the area under the Voigt curve. The measured area under the spectral line, along with the pressure, temperature, and line strength, are used in conjunction with the ideal gas law and the Beer-Lambert law to find the HCl concentration, which is given by:

$$[HCl] = 10^6 \frac{T}{P} \frac{k_B}{S} \frac{A}{L_{eff}}, \tag{4}$$

where T is the temperature of the intra-cavity gas in K, P is the pressure in Pa, k_B is Boltzmann's constant in J K^{-1}, A is the area under the spectral line in cm^{-1} (discussed below), S is the line strength in cm $molecule^{-1}$, and L_{eff} is the effective path length in cm. The area under the spectral line, A, is the integral of the dimensionless cavity loss $\left(\frac{L}{c\tau}\right)$ over frequency in cm^{-1}. For CRDS systems in which the interrogated sample fills the entire region between the mirrors, the effective path length is the same as the physical distance between the cavity mirrors. However, as can be seen in Figure 9, the cavity inlet and outlet flows are connected over a shorter path than the mirror separation distance, and a nitrogen purge (flow rate of 0.4 slpm) is introduced in the cavity at each mirror surface in order to prevent particles from contaminating the mirror surfaces. To compensate for the diluted sample, an effective path length replaces the cavity length in Eqn. 2 [93]. To determine the effective path length, the laser wavelength was tuned to the nearby water absorption line in Figure 8 and the area of this spectral line was found with the purge flow on and off. The physical path length (mirror separation) was multiplied by the ratio of these areas, yielding an effective path length of 86% of the physical length, which approximately matches the length between the sample inlet and outlet ports.

Details of the flow system are shown in Figure 11. As previously mentioned, the system is run at 0.1 bar to ensure separation between spectral features.

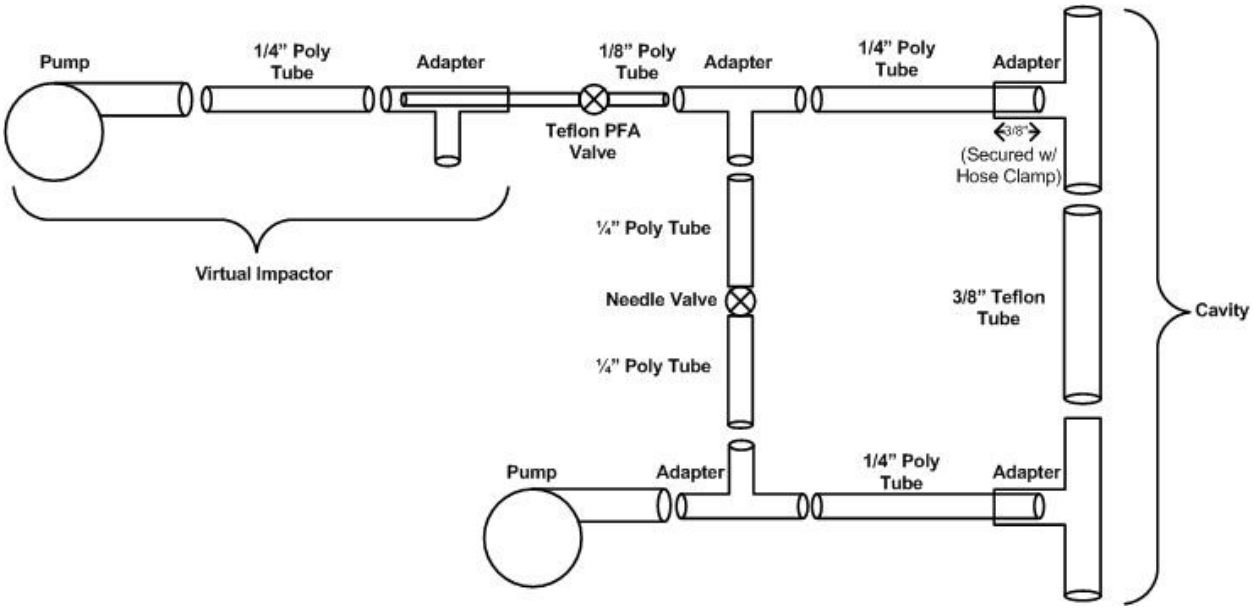

Figure 11 - Schematic diagram of the HCl sensor gas flow system. The virtual impactor, indicated on the left, serves to remove large particles from the main sampling flow. The optical cavity is indicated on the right.

A vacuum was pulled on the system by a dry scroll pump (Varian, IDP2B01) and cavity pressure was regulated by a combination of a needle valve in the bypass leg and Teflon® needle valve near the intake. The same combination of valves was used to set the flow rate of sample through the cavity to 4 slpm, including the purge flow.

The system also employs a simple virtual impactor to remove large particles from the main sampling flow. Not only are large particles in the sample flow threatening to the highly reflective mirror surfaces, but they can scatter or absorb intra-cavity light, increasing the variance in the ring-down time. An inline filter cannot be used in this case, as HCl strongly adsorbs to surfaces, and will barely transmit through the filter. Instead, the virtual impactor acts as a particle filter by requiring the flow to quickly turn 180 degrees before being routed to the cavity. The design requires the flow to be split into two legs as shown in Figure 11.

Due to its strong dipole moment, HCl has a high propensity to adsorb to surfaces, which constrains the instrument design and limits the detection time response. The adsorption can be

partially mitigated by reducing the surface area of the flow system and cavity, and by using Teflon® components. Perfluoroalkoxy, or PFA, a type of Teflon®, was the fluoropolymer of choice because components can be injection molded from PFA resulting in less porous surfaces than other fluoropolymer pieces forged from a powder, such as polytetrafluoroethylene (PTFE). Other cavity-enhanced detection techniques, such as off-axis Integrated Cavity Output Spectroscopy (ICOS), suffer in time response from the need for increased intra-cavity surface area. Additionally, the inlet and cavity tubing are heated to 60^{o} C, which causes surface desorption of the HCl to occur faster, and reduces the amount of moisture available to trap HCl. It was shown by Roberts et al [26] that even using short lengths of extruded (nonporous) fluoropolymer tubing will adsorb HCl resulting in an instrument response time of greater than 90 seconds.

2.2 SENSOR PERFORMANCE

This section discusses validation studies and performance metrics for the HCl sensor. Section 2.2.1 focuses on the base optical sensitivity and the limit of the detection of the instrument. Section 2.2.2 gives the validation data obtained from a calibrated source. Examples of ambient HCl concentration measurements from a field study are given in section 2.2.3.

2.2.1 LIMIT OF DETECTION

The detection limit of a CRDS sensor for measuring trace atmospheric species depends on the instrument's optical sensitivity as well as the spectroscopic relation between the optical absorption and species concentration. Optical sensitivity is generally described in terms of the

noise-equivalent absorption, k_{Min}. For cw-CRDS systems, k_{Min} values of ~10^{-10}–10^{-12} cm^{-1} can be achieved, as has been described in review articles [45], [94]. The minimum detectable absorption can be evaluated from experimental parameters as [95]:

$$k_{min} = \left(\frac{\Delta\tau}{\tau}\right)_{Min} \frac{(1-R)}{L} \tag{5}$$

where $(\Delta\tau/\tau)_{Min}$ is the minimum measurable fractional change in the ring-down time (typically limited by technical noise). While longer integration times generally lead to reduced $\Delta\tau/\tau$, and improved sensitivity, eventually system drift dominates such that there is an optimum (finite) integration time. In order to find the ideal integration (averaging) time for the presented CRDS system, an Allan Variance study was performed using the modified method of Huang *et al.* [96]. While the algorithm presented by Huang gives the same information as the traditional Allan Variance, the available data is essentially averaged more, yielding a much smoother Allan Variance curve. Figure 12 (top plot) shows a sample ring-down data set with the optical cavity purged with ultra-zero air (purity~99.9997%).

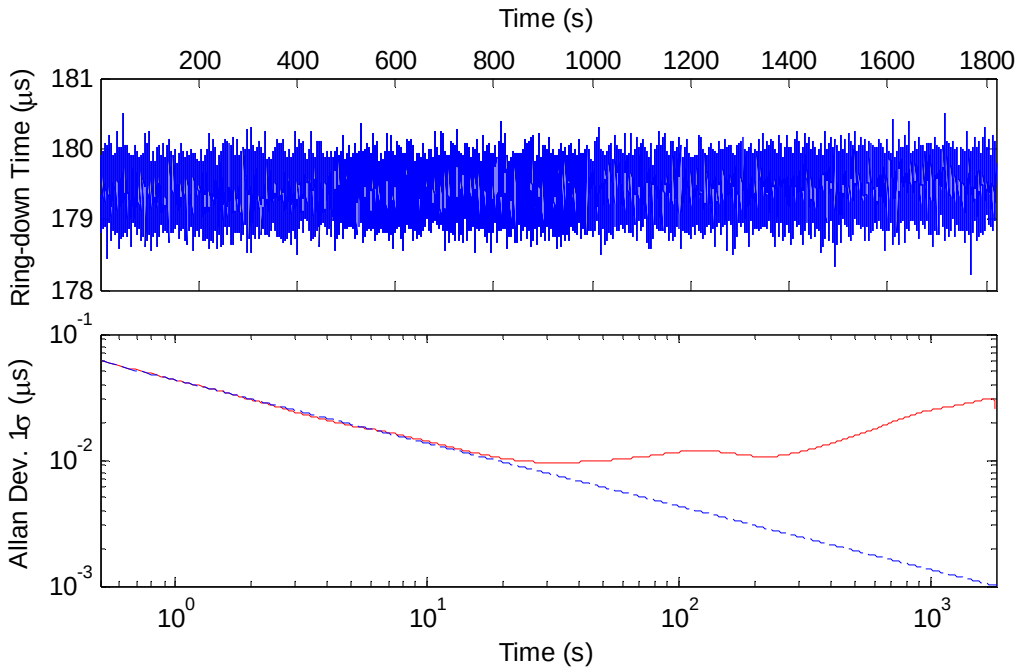

Figure 12 - (Top) Sample ring-down data when the optical cavity was purged with ultra-zero air. (Bottom) Modified Allan Deviation of the ring-down data (red solid line) as compared to the idealized data without drift, i.e. time-1/2 dependence (blue dashed line).

The minimum in the Allan Variance of ~0.01 μs (bottom plot), which occurs at an optimal integration time of ~30 seconds, divided by the mean ring-down time, gives $(\Delta\tau/\tau)_{min}$ of 5.3×10^{-5}. Using R=0.99982 and L=90 cm, results in an optical sensitivity (1σ) of 1.1×10^{-11} cm^{-1} in 30 seconds. From the HITRAN spectral simulations discussed earlier, an optical sensitivity of 1.1×10^{-11} cm^{-1} corresponds to a theoretical HCl detection limit of 10 pptv. The aforementioned value would apply if the laser were fixed at a single frequency on the spectral line peak. Due to practical considerations, such as drifting cavity loss and changing laser frequency, the laser is swept over of the broadened spectral line, thereby capturing the baseline, but at the cost of lower detection sensitivity. Based on the optimal integration time of 30 seconds, a HCl concentration

measurement was also performed while purging the cavity with ultra-zero air, as shown in Figure 13.

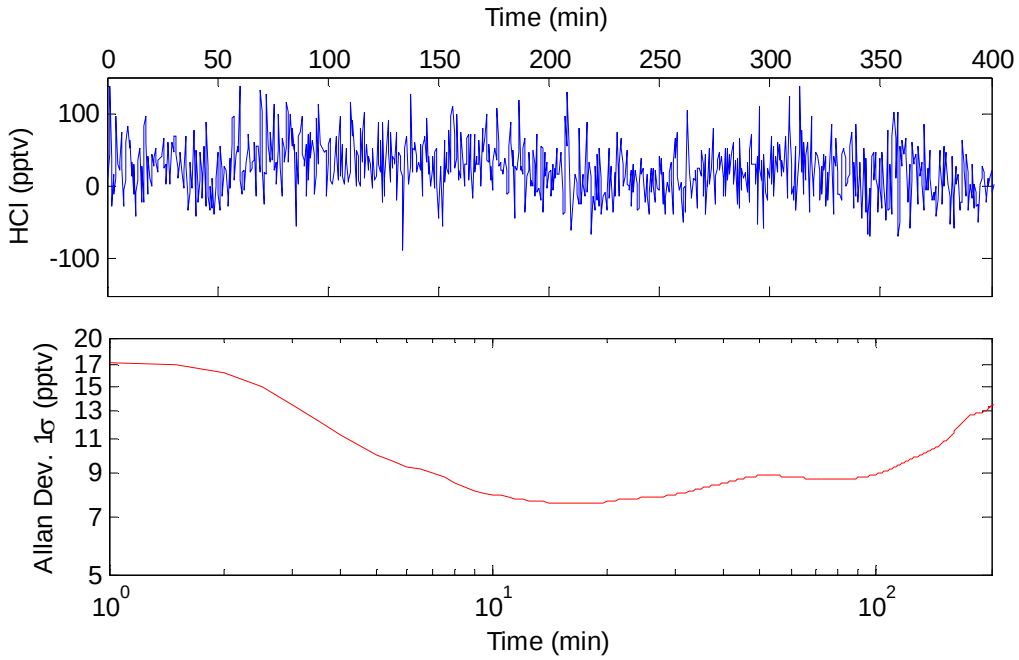

Figure 13 - Measured HCl concentration values (top) and their associated Allan Deviation curve (bottom) with the optical cavity purged with ultra-zero air.

The modified Allan Variance algorithm discussed earlier was also used to find an HCl limit of detection of 17 pptv (1σ) after 1 minute and 10 pptv (1σ) after 5 minutes. These sensitivity (precision) values compare very favorably against the typical atmospheric abundances that the instrument is designed to measure (10s-100s of ppt to several ppb, see Section 1.2). The sensitivity of the present instrument is somewhat better than that of past work using infrared lasers and Herriot cells (~100 ppt in 30s [31]) with the main differences being that the current work allows several orders of magnitude better optical absorption sensitivity (owing to the use of CRDS versus multi-pass cells), but probes weaker lines (2-0 band as opposed to 1-0 band). From a practical point of view, the present instrument has the important advantage of using uncooled

NIR diode lasers as opposed to lead-salt lasers implemented by Scott *et al.* that require LN2 cooling.

2.2.2 VALIDATION DATA

Given the directly quantitative nature of CRDS, typical calibration studies are unnecessary; however a test with an HCl calibration source was performed in order to validate the accuracy of the instrument. Figure 14 shows a schematic of the calibration source, which consists of permeation tube containing hydrochloric acid.

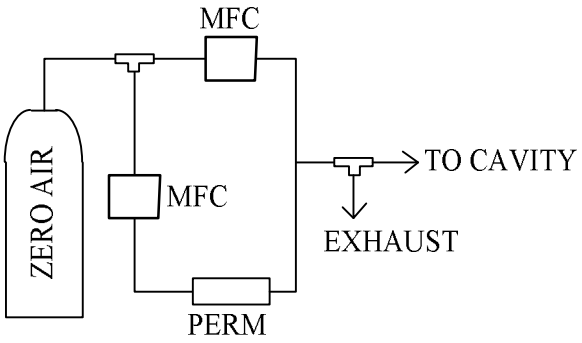

Figure 14 - Schematic of the HCl calibration system. MFC: Mass Flow Controller, PERM: Permeation Tube.

The tube emits gaseous HCl at a rate of 10 +/- 1 ng/min, when temperature controlled at 55^{o}C. Ultra-pure zero air (Airgas, 99.9997% pure) flows over the permeation tube at a rate of 9.9 sccm, giving an HCl concentration of 630 ppbv. The flow from the permeation tube is further diluted by a few slpm of zero air at a rate set by an adjustable mass flow controller, thereby allowing the final HCl concentration to be set.

Past work has shown the design of a fast-response inlet and flow system for HCl is very challenging and requires careful consideration of flow-rates, materials, and geometry (owing to gas adsorption effects). Roberts *et al.* reported challenges in appropriate HCl inlet design in their CIMS instrument including inlet equilibration times of ~90 s [26]. Early work, using a glass cell, required 30 minutes for the concentration to equilibrate to new values, which corresponded to ~60 cell flushes based on residence times [97]. The past work with optical measurements in Herriot cells found response times of 10s of seconds and emphasized the importance of having a high flow rate [30].

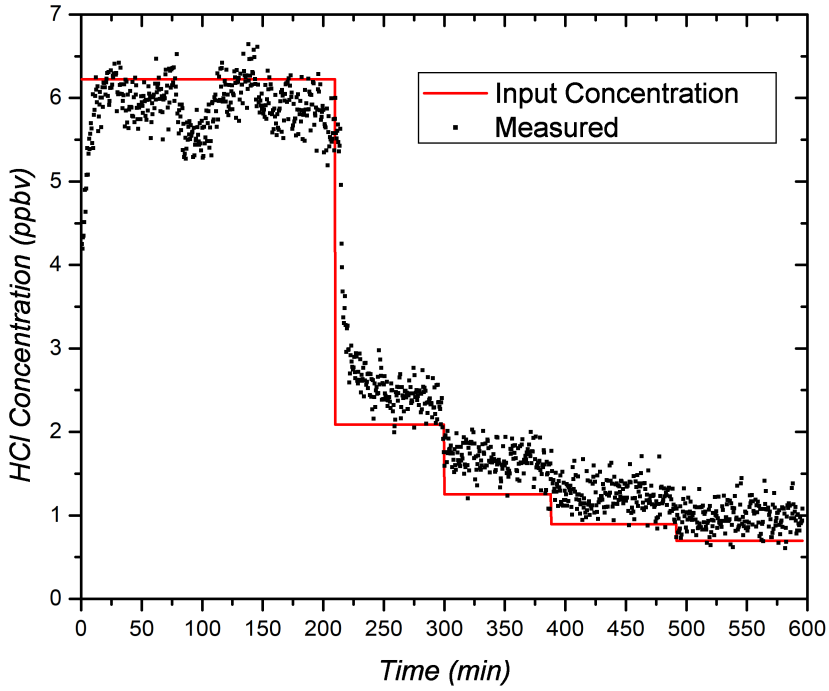

Figure 15 - Step-down study of HCl concentration showing measured concentrations versus time. The actual input concentrations are also shown with the solid line.

The time response of the measurement system has been characterized by examining the measurement settling time during a step-down study with the permeation tube source (Figure 15) where the input concentration was reduced in a series of steps. The signal change can be well fit with a decaying exponential with 1/*e* time constant of 4 minutes. The time is considerably longer than the transit time through the cell (estimated as ~10 s based on flow parameters) meaning that multiple flushes are required (similar to the findings of Fried [97]). Past measurements with similar ring-down systems but for non-sticky gases, show measurement settling times much closer to the residence time. While the 4-minute time response is adequate for some monitoring applications, future work will aim to improve it by increasing the flow-rate and cell wall temperature [30].

Figure 16 shows averaged data from Figure 15. A 10 minute average was taken from the center of each input step, and plotted against the input concentration.

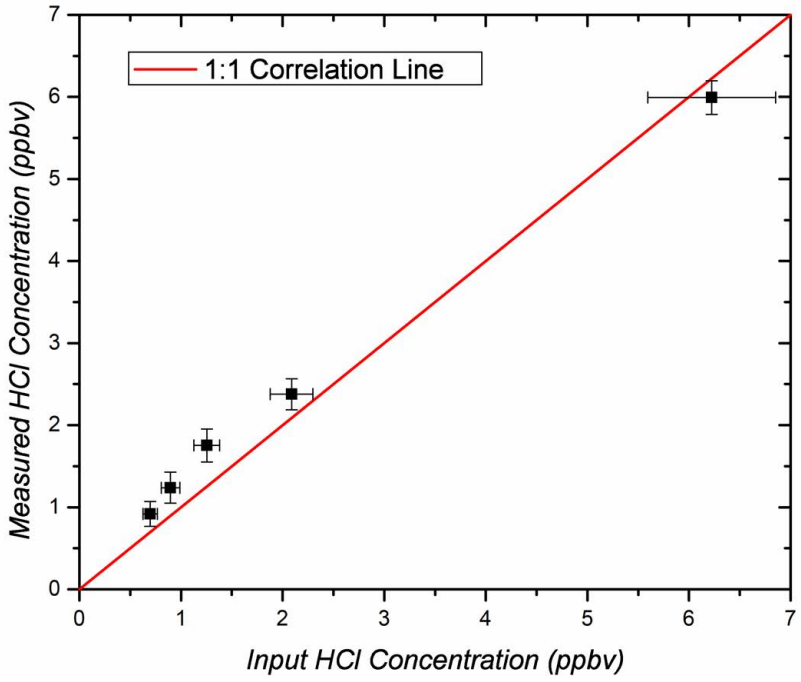

Figure 16 - HCl concentration measurements averaged for 10 minutes as compared to the concentration supplied to the inlet from the calibration system. The solid line shows the expected 1:1 correlation between the measured and input values.

The solid line shows the ideal 1:1 correlation. The errors bars in the input concentrations are due to a 10% uncertainty in the calibration source, while errors bars on the measured concentration are taken as the (1σ) standard deviation in the measured values during the 10 minute averaging time. There are not any obvious systematic error, for example as would be the case if the assumed linestrength were incorrect, and generally observe consistency of better than 10% between the expected and measured values. The 10% accuracy is essentially the same as that reported in past work using lead salt lasers and Herriot cells [31].

2.2.3 FIELD STUDY DEMONSTRATION

The first field test of the presented CRDS instrument was during the nitrogen, aerosol composition and halogens on a tall tower (NACHTT) campaign, in Erie, Colorado during early 2011. Although the instrument was still early in its development, the field campaign provided an opportunity to run our instrument side-by-side with two other instruments employing different HCl measurement methods. The first method being organic acid CIMS, [27] and the second method being mist chamber ion-chromatography [98].

Located within a box truck, the CRDS instrument collected air samples from the base of the Erie tower. The mist chamber ion-chromatography instrument was also located at the tower base, while the acid CIMS instrument traveled in a carriage up and down the tower. HCl concentration measurements taken by the three HCl instruments are compared in Figure 17.

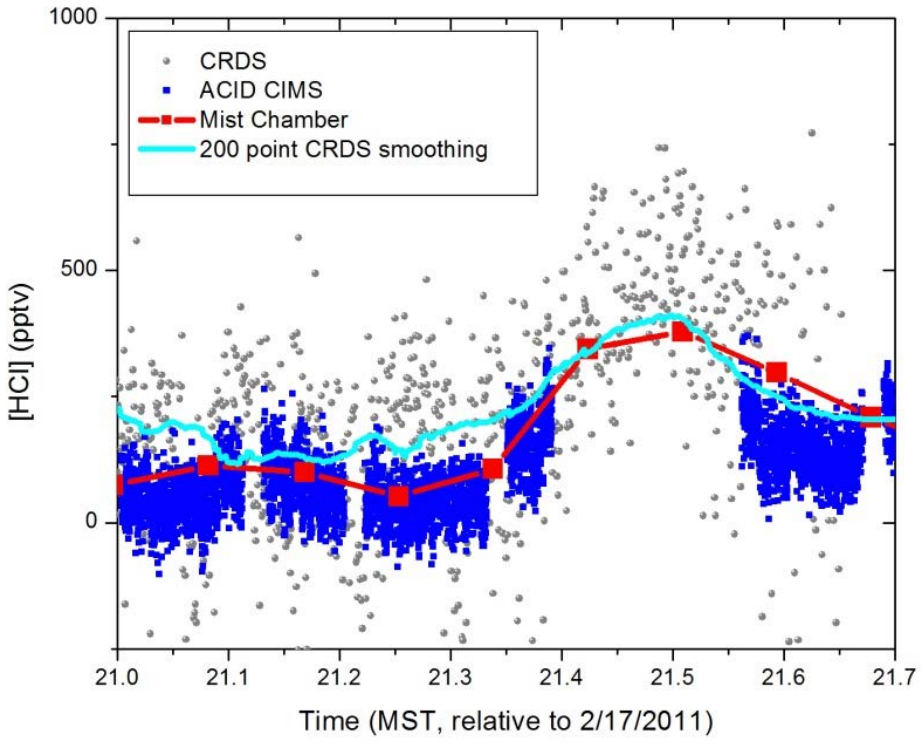

Figure 17 - HCl concentration values recorded by the CRDS, ACID CIMS, and mist chamber instruments during the NACHTT campaign.

The sample data set, taken around 21:30 MST on Day 21 (February 17, 2011) of the study, shows agreement between the three instruments, including observation of a plume containing ~500 pptv of HCl.

3. CAVITY ENHANCED ABSORPTION SPECTROSCOPY INSTRUMENT FOR AEROSOL EXTINCTION MEASUREMENTS

A novel broadband cavity enhanced absorption spectroscopy (CEAS) laser-based instrument to measure the extinction component of aerosol SSA has been developed and undergone a preliminary characterization. The instrument uses a supercontinuum light source coupled into a high finesse prism retroreflectors optical cavity to make sensitive measurements of aerosol optical extinction. In order to test the cavity enhanced detection, a solution of ammonium sulfate and nigrosin dye dissolved in deionized water was introduced into the aerosol flow system. For a 43-cm cavity length, a minimum detectable extinction coefficient of 8×10^{-8} cm^{-1} for 10 ms collection time was obtained. The remainder of this chapter discusses the design and development of the aerosol instrument.

3.1 OPTICAL SETUP

Described here is the approach and setup for the broadband measurements of optical aerosols. The schematic of the optical system is similar to that shown in Figure 5, however, a more detailed diagram of this configuration is shown in Figure 18

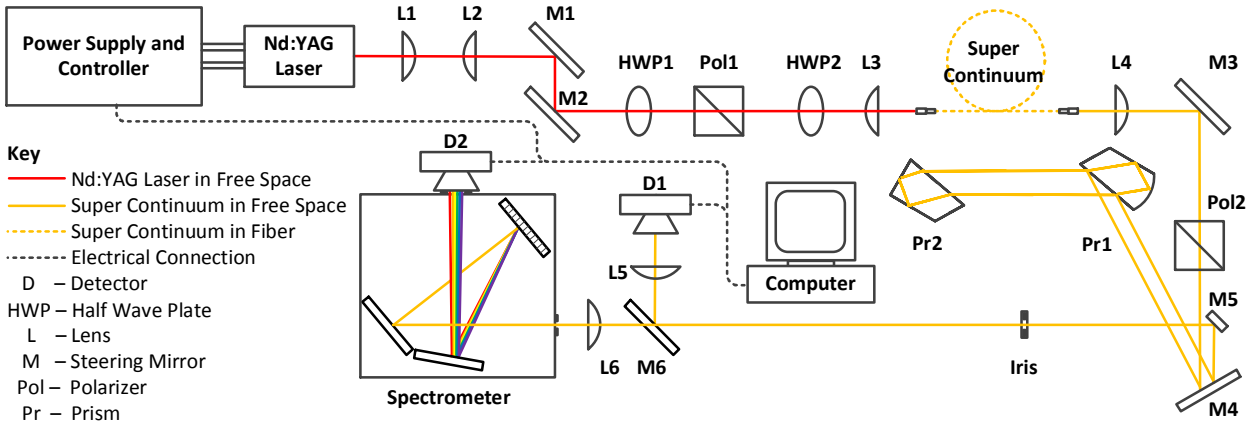

Figure 18. Schematic of optical components for the aerosol CEAS sensor.

Following prior research, a custom laser pumped supercontinuum setup is employed to provide the broadband light source. The pumping laser is a Nd:YAG (1064 nm) source operated at repetition rate of 20 kHz with pulse duration of ~24 ns, and pulse energies of ~40 μJ (corresponding to average power of 0.8 W, and peak power of 1.7 kW). The first three lenses downstream of the laser source (*L1*, *L2*, and *L3*) were selected and positioned to optimize the supercontinuum fiber (NKT Photonics, SC-5.0-1040-PM) launch conditions and, therefore, maximize fiber transmission. The half-wave plate and polarizer combination (*HWP1* and *Pol1*) act as a variable attenuator and allow the user to finely adjust power in the optical setup. A half-wave plate (*HWP2*) downstream of the variable attenuator aligns the laser to the polarization axis of the fiber in order to increase transmission. To avoid damage to the supercontinuum fiber, the (average) input power is limited to ~0.7 W which provides a total output power of ~0.3 W, spanning to ~500 nm on the blue side, approximately consistent with past research using similar nanosecond laser sources and fibers [86]. An example of a supercontinuum spectrum from this setup is shown in Figure 19.

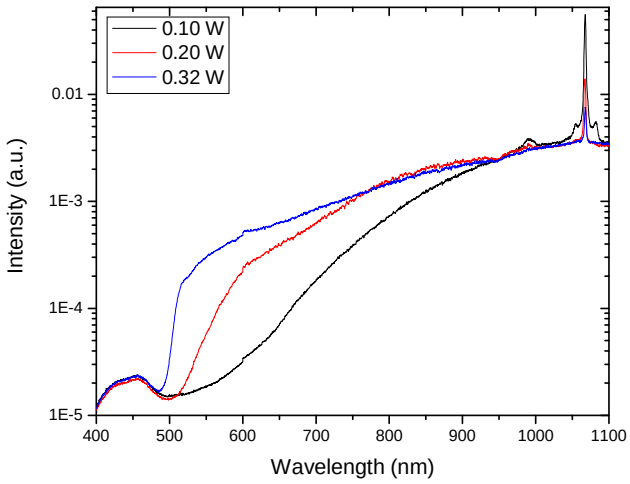

Figure 19 - Spectrum of the supercontinuum fiber-pumped light source for three different output powers.

As seen in the previous figure, significant levels of 1064 nm pump light remain in the supercontinuum output. This phenomenon was studied by Dr. Kevin Lehmann's group who measured up to thirty five percent of residual 1064 nm light for a variety of laser repetition rates. Although the spectrometer (which will be described later) effectively filters this component, the ~0.3 W total output power is not an accurate representation of the visible power used in this experiment. For high-sensitivity detection, it is important the supercontinuum spectrum (overall amplitude and shape) be stable, and a number of characterizations were performed over different timescales, finding typical stability of ~1% (fractional variation at middle visible wavelengths) over timescales of seconds.

Prior to measuring aerosol absorption, the finesse (reflectivity) of the optical cavity was studied as well as the system's overall extinction sensitivity. The optical cavity employs precisely constructed and polished fused silica retroreflector prisms following past designs from Lehmann *et al.* [81]. The prisms are employed in a two-prism (*Pr1* and *Pr2*) linear cavity of

length 43 cm, to which the beam was spatially mode-match using an optical profiler to determine the beam sizes and q-parameter Gaussian beam propagation calculations. In this optical setup, the beam is mode-matched to the prism cavity only in the sagittal plane (perpendicular to the tangential plane formed by the incident and reflected rays). This setup is, therefore, quite different than the reflective optics based astigmatic mode-match presented in Figure 5. Although an astigmatic mode-match setup was also designed and constructed (Figure 20), the non-astigmatic (stigmatic) configuration was used as it is much less complicated.

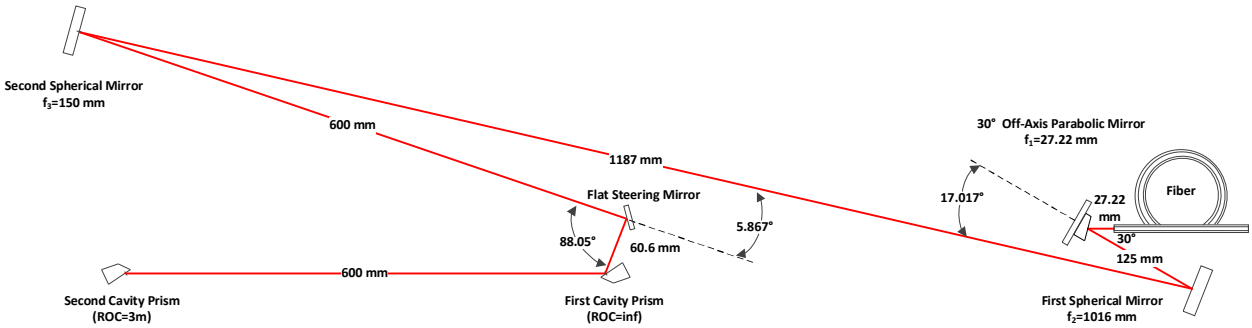

Figure 20. Example astigmatic mode-match solution using reflective optics (not used).

In order to spatially mode-match with refractive optics, an achromatic doublet (Thorlabs, AC050-008-B-ML) is precisely positioned downstream of the fiber output (*L4* in Figure 18), satisfying cavity mode-match in either the sagittal or tangential plane. Determining which cavity plane to mode-match was arbitrary since a better solution might be to determine the fiber to lens distance needed to mode-match in each plane and split the difference. The use of an achromatic doublet is essential to the mode-match because unlike standard lenses, an achromatic doublet focuses light of various wavelengths (critical for a supercontinuum light source) to approximately the same point. An astigmatic setup would yield a better spatial mode-match and

in theory, lead to higher finesse; however, the simple stigmatic solution presented here is sufficient to achieve high instrument sensitivity (see 3.1.1). Finally, a high extinction broadband polarizer (Thorlabs, GL 10) is placed downstream of the achromatic doublet to set the polarization of the light entering the cavity.

Prior work in gas-phase spectroscopy, for example to obtain the spectrum of Figure 6, employed a relatively high-resolution detection system but over a small spectral extent of only several nanometers. For the aerosol detection high spectral resolution is not required, since the absorption features are not sharp as in the gas-phase, but a much broader spectral extent of hundreds of nanometers is necessary. A low-resolution spectrometer (Oriel, 77400 MS125 MultiSpec Spectrograph + Oriel, 78854 CCD) is used to simultaneously detect light in the ~400-975 nm range with 1-nm wavelength resolution and high throughput. (These parameters are achieved with a diffraction grating of 400 lines per mm, blazed for 500 nm, slit width of 120 μm, and binning 4 CCD pixels for each channel.) The CRDS method of measuring ring-down times is implemented to characterize the prism reflectivity and cavity finesse. Since the prisms are aligned using the 1064 nm pump beam, an InGaAs detector (New Focus, 2053) is used in conjunction with the HCl CRDS labview program (described in 2.1) to instantaneously measure ring-down time. This detection setup (*M6*, *L5* and *D1*) is extremely helpful for optimizing prism alignment and has achieved ring-down times of 12 μs (corresponding to R=0.9999 for the 43-cm length cavity). When the supercontinuum light source is directed through the optical setup, a different detection system must be implemented. In order to isolate the behavior at different wavelengths, the (post-cavity) light is dispersed through the monochromator, but the CCD is replaced with a photomultiplier tube (Hamamatsu, R9110)/slit assembly to capture the time-dependent ring-down signals. Ring-down times at several wavelengths were determined (Figure

21): for example, a ring-down time of 4.3 μs at 575 nm was found, corresponding to *R*=0.9997 for the 43-cm length cavity. (Past work, with higher wavelength resolution required a multi-channel scaler to build up photon counts and measure ring-down traces, but that is not required here given the high photon counts in the broader wavelength channels.)

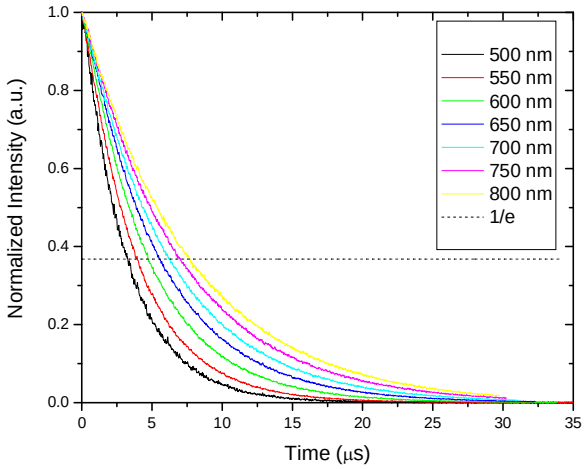

Figure 21 - Ring-down traces at different wavelengths from the broadband extinction system.

The vendor who provided the prisms (Tiger Optics) performed similar characterizations and found somewhat higher reflectivities (e.g. R=0.99996 at wavelength of 1600 nm) which indicates that, with further improvements in mode-matching and alignment, better performance is expected (though higher reflectivities are normal at the longer wavelengths owing primarily to reduced scatter loss).

3.1.1 OPTICAL SENSITIVITY

For assessing instrument performance, the (extinction) sensitivity of the current system was estimated from the fluctuations of the baseline signal (with no sample present) and the cavity reflectivity. From the fractional standard-deviation in the baseline noise of ~0.010, and the mirror reflectivity of 0.9997 (cavity enhancement factor of *1/(1-R)=3070)* a minimum detectable absorbance of 3.3×10^{-6} was determined. These values are for CCD integration time of 10 ms, yielding a theoretical minimum detectable absorbance of 3.3×10^{-7} for 1-s measurement times (assuming shot-noise limited square-root scaling as typically holds for time durations up to minutes [82]). Finally, for the 43-cm cavity length, a minimum detectable extinction coefficient of 8×10^{-8} cm^{-1} for 10 ms collection time was obtained [99]. In theory, this sensitivity can be extrapolated to a 1-s collection time yielding a minimum detectable (noise-equivalent) absorption coefficient of 8×10^{-9} cm^{-1} $Hz^{-1/2}$ (equivalent to 0.8 Mm^{-1} for 1-s collection time). This extrapolated sensitivity is slightly better than that of Lehmann's past published work (7.2×10^{-8} cm^{-1} $Hz^{-1/2}$), which is to be expected given that there are more detected photons per wavelength-channel in the current broadband system.

3.2 OPEN AEROSOL DELIVERY SYSTEM

For initial feasibility measurements a simple, open aerosol delivery system shown was implemented (Figure 22).

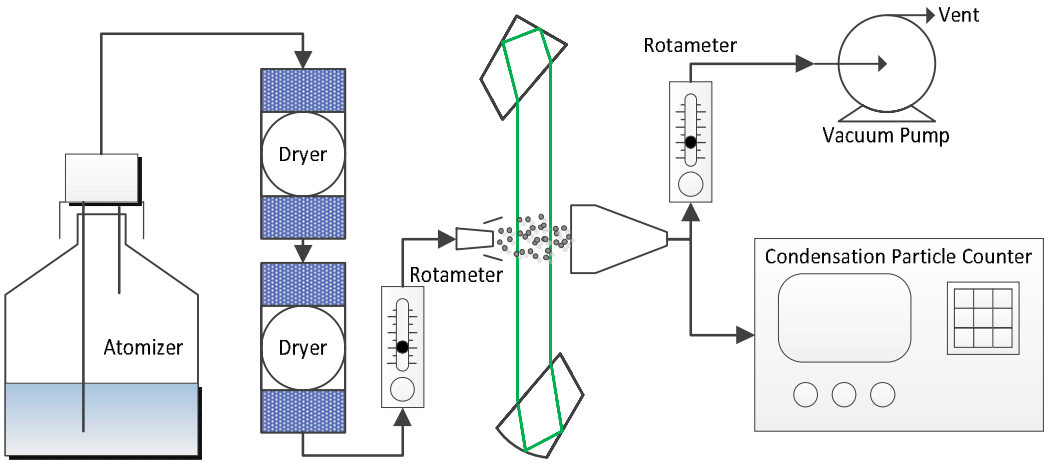

Figure 22 - Simplified aerosol generation and delivery system used for “proof of concept”.

The aerosol system comprises a constant output nebulizer (TSI 3776) connected to pressurized zero-air with output flowing through two diffusion dryers and then across the optical cavity – for an initial “proof-of-concept” a closed flow system for the cavity was not developed, rather the aerosol output flow is directed (exiting a tube of diameter 0.5 cm) across the optical axis. For calibration of the aerosol concentration, the aerosol flow is “caught” by a slightly larger diameter suction tube that passes the aerosol flow to a particle counter (TSI Ultrafine Condensation Particle Counter (CPC) - 3776). Future instrument implementation will use a more sophisticated (enclosed) flow system as described in section 4.2.

3.2.1 BROADBAND AEROSOL MEASUREMENT

In order to test the cavity enhanced detection, a solution of ammonium sulfate and nigrosin dye dissolved in deionized water was introduced into the aerosol flow system depicted in Figure 22. The original solution before dilution was characterized by 1 g of ammonium sulfate and 0.3 g of nigrosin in 1 liter of deionized water, with the nigrosin added to increase the

optical absorption of the test aerosol. This mixture was sequentially diluted with deionized water prior to atomization in order to measure the dependence of aerosol extinction on wavelength as a function of aerosol number concentration. The intensity spectrum was measured for the various dilutions ($I(\lambda)$) as well as for a reference spectrum of pure water ($I^o(\lambda)$). Using interpolated values of ring-down time from Figure 21 in conjunction with equation (1), the measured intensity spectra were converted into extinction coefficient as seen in Figure 23.

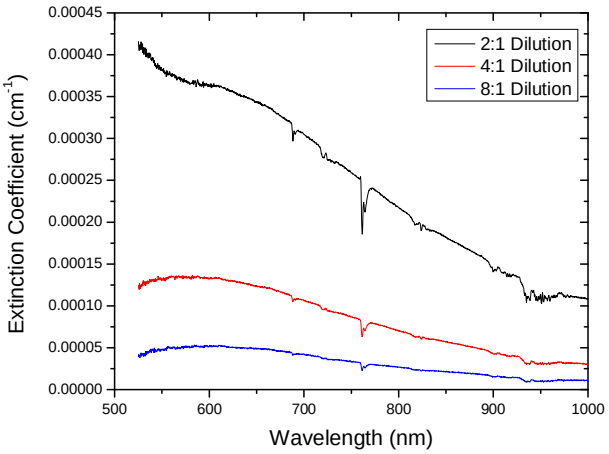

Figure 23 - Aerosol extinction spectra measured with traces at different wavelengths, from the broadband extinction system.

These signals are large relative to our detection limits (see below) and these spectra could be accumulated with very short integration times (<<1 s). Because a closed flow system (i.e. a setup that filled the cavity with aerosol flow) had not been developed by this point in the project, the background gas absorption features could not be properly subtracted. For this reason, absorption features of molecular oxygen (A-band) and water are visible at ~760 nm and ~940 nm respectively. While not ultimately desired, the features do further confirm the wavelength axis

and absorption measurement. (Note that because of the relatively wide wavelength resolution of the system the peak absorption of these features is less than it would be with a narrow line system, and that the features show up inverted since we have referenced the aerosol data, where the stream fills only part of the cavity, against data from the air filled cavity.)

3.3 CLOSED AEROSOL DELIVERY SYSTEM

The simplicity of the open aerosol delivery system was useful for proof-of-concept measurements; however, a more sophisticated closed aerosol test apparatus has since been developed (Figure 24) in order to more effectively control aerosol distribution across the CEAS sensing region. Note that, in contrast to similar linear flow cells used for mirror-based CRDS or CEAS, the need to align prisms requires a more "open" design. This test apparatus will be discussed in great detail for the remainder of this section.

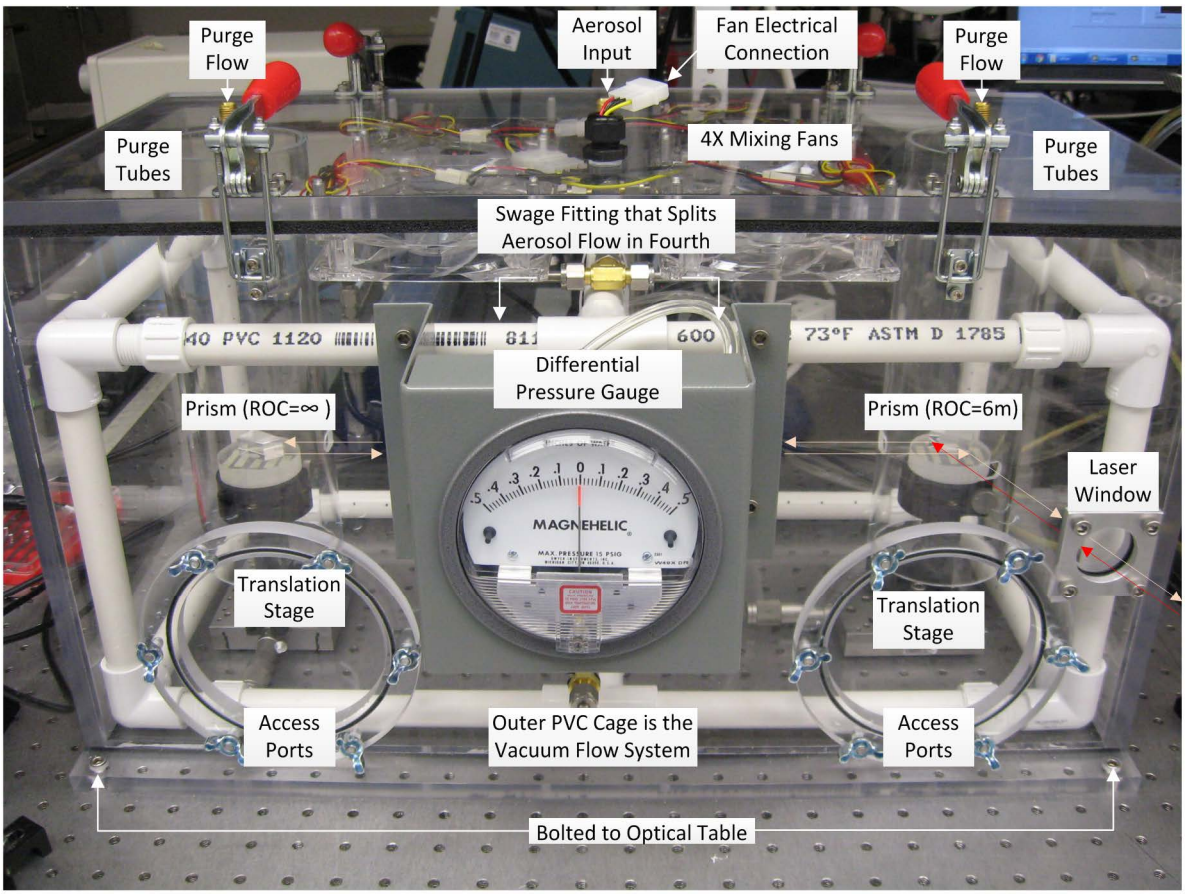

Figure 24. Closed Aerosol Test Apparatus.

3.3.1 APPARATUS DESCRIPTION

The outer structure of the apparatus is made of 1.25 cm (0.5”) thick clear acrylic which was chosen for its ease of machining as well as low cost and availability. In the aerosol research community, the use of acrylic (or any plastic for that matter) is generally avoided since particle losses tend to be large. The loss mechanism is governed by the flow of aerosols over plastic which creates a static electric buildup. Since many particles carry charge (generally the larger the particle, the higher chance the particle carries charge), they are attracted to the charged surface and effectively removed from the aerosol bulk volume. This is problematic since it

creates a steep concentration gradient extending out from the charged surface. Regardless, this loss mechanism is negligible for this test apparatus since the prisms are suspended in the center and are conveniently far removed from plastic surfaces. When aerosol is first introduced into this test fixture, there will be aerosol loss due to the plastic structure; however, the concentration of the atomizer solution can be increased to remedy this issue. The acrylic structure is welded together in order to effectively seal the system and keep the aerosol sample within the test apparatus.

The optical setup is nearly identical to the one described in 3.1 with the minor exception of an UV fused silica window (Thorlabs VPW42) upstream of the first prism. The purpose of this window is to merely allow the laser to be directed unperturbed into test chamber all the while maintaining the seal of the system. The window has been positioned relative to the incidence beam in order to minimize its etalon and dispersive effects. Since the window is held against an o-ring groove assembly with a retaining plate, birefringence can be induced by putting too much stress on the optical window. The birefringence can lead to a significant drop in ring-down time since the window is downstream of the polarizer. Theoretically, any issues related to the window could be solved by placing the polarizer downstream of it, however, the layout of the current test apparatus does not allow for this rearrangement. Regardless, the test structure can be sealed with minimal amounts of birefringence induced.

The aerosol flow system has been designed to maximize aerosol mixing with the intent of achieving a constant aerosol concentration distribution throughout the test apparatus. The flow system is comprised of six major components: (1) aerosol flow, (2) purge flow, (3) dilution flow, (4) vacuum flow, (5) differential pressure gauge, and (6) mixing fans. Aerosol (the creation of which will be discussed later) is introduced into the test apparatus through the center of the lid

(see Figure 24 for a better visual representation). Once the aerosol enters the case, a Swagelok fitting splits the aerosol flow into four legs in order to promote mixing. The condensation particle counter (CPC) pulls an aerosol sample out of the test apparatus via an electrically conductive tube placed near the CEAS sensing region. It is important to note that the length of tube between the aerosol sample and CPC is known so that diffusion losses can be calculated leading to corrected concentration measurements. The purge flow, a preventative measure to keep the prisms clean, is comprised of two acrylic tubes that are welded to the lid of the aerosol case and therefore, "hang" over each prism stage assembly. Holes were strategically drilled into these purge tubes to allow for the laser to pass through them uninterrupted. Both purge tubes are kept at weak positive pressure using a nitrogen tank in order to keep any aerosol in the test apparatus from adhering to the high finesse prisms. In Figure 25, the outer PVC tubing system is all connected to a vacuum pump (green lines) whereas the inner ring is connected to a dilution air supply (blue lines).

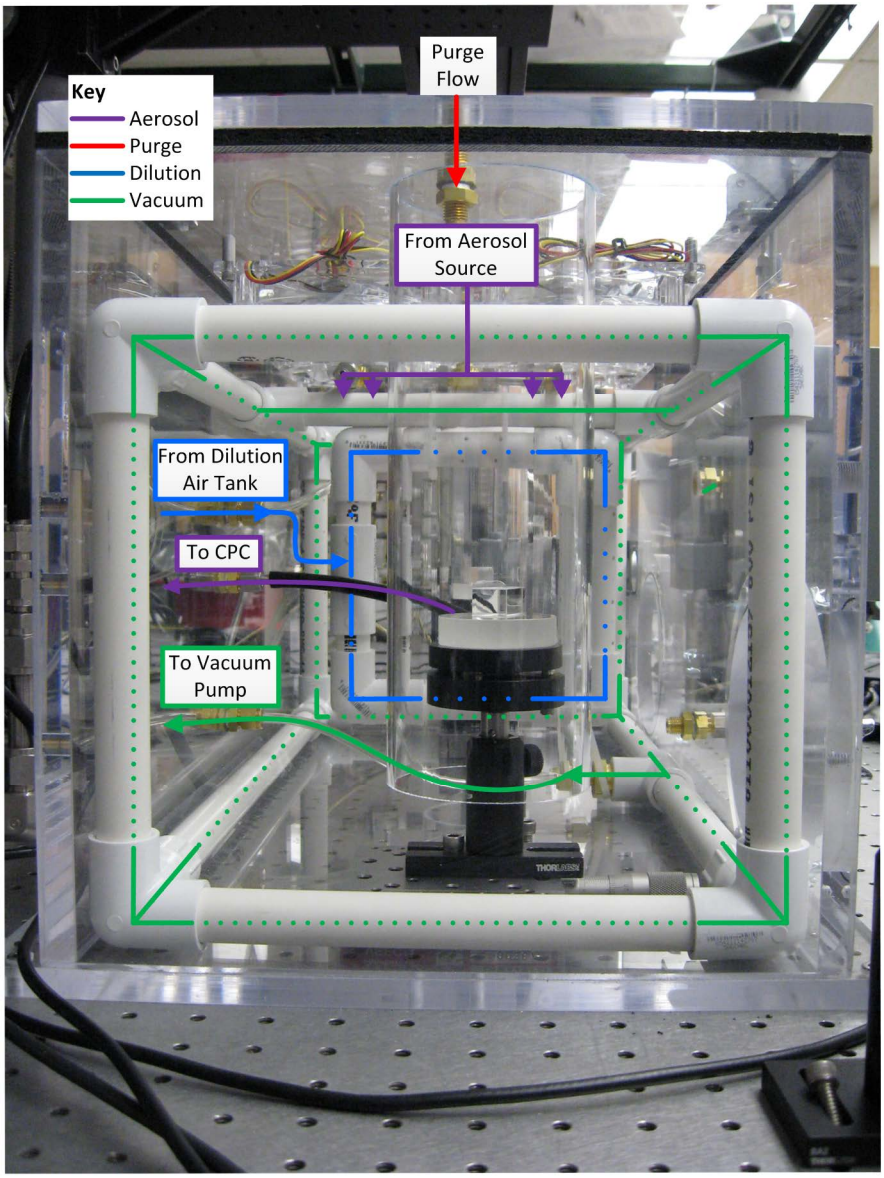

Figure 25. Flow system of closed aerosol test apparatus.

The dilution flow allows the user to change the aerosol concentration by means of diluting the fixed concentration of the aerosol source. When aerosol, dilution, and purge flow are all used, the vacuum flow is set to balance the total input and output flows at the same flow rate. This concept is analogous to the "throw and catch" method described in 3.2 and therefore, aerosol is continuously flowing in and out of the system. The tubes for both the dilution and vacuum flow

systems have multiple holes systematically drilled in them to make the aerosol distribution spatially uniform throughout the test apparatus. Furthermore, the total outlet area of dilution and vacuum flow system are nearly identical in order to keep the pressures within both sets of tubing the same. To exactly balance the flows in and out of the system, a differential pressure gauge (Dwyer, 2301 Magnehelic Gauge) and generic needle valves has been implemented. Finally, four computer fans (mounted to the lid) are used to mix all of contents found in the test apparatus, again with the purpose of creating a spatially uniform aerosol distribution.

3.3.2 PRELIMINARY CHARACTERIZATION

The closed aerosol test apparatus was developed after the proof-of-concept phase and has not been fully characterized. Nevertheless, the remainder of this section is devoted to initial analysis of this test chamber. The prisms have been successfully aligned with a comparable ring-down time of 12 μs (corresponding to R=0.9999 for the 43-cm length cavity). A solution of ammonium sulfate was introduced into the aerosol delivery system; as expected, ring-down time decreased slowly as concentration converged toward an equilibrium state. However, when the aerosol supply was stopped, the ring-down times did not return completely to their initial value. This observation is consistent with the possibility that the prisms were slowly getting covered in a layer of aerosol (the prisms were later cleaned and ring-down time returned to 12 μs). Ring-down time decay is problematic since the user cannot readily decipher the difference between aerosol extinction and prism degradation in the output signal. Currently, efforts are being made to improve the purge flow system and keep the prisms clean. Even though this preliminary test may seem inconclusive, time decay of the test apparatus was determined using the CPC. As seen

in Figure 26, the ammonium sulfate concentration decay was measured when the aerosol supply was disconnected from the test apparatus. An exponential trend line was fit to the data, allowing for the 1/*e* time constant to be calculated as ~100 seconds. This value is lower than one found for the HCl sensor (<250s) but from sampling perspective, reducing this value would be beneficial.

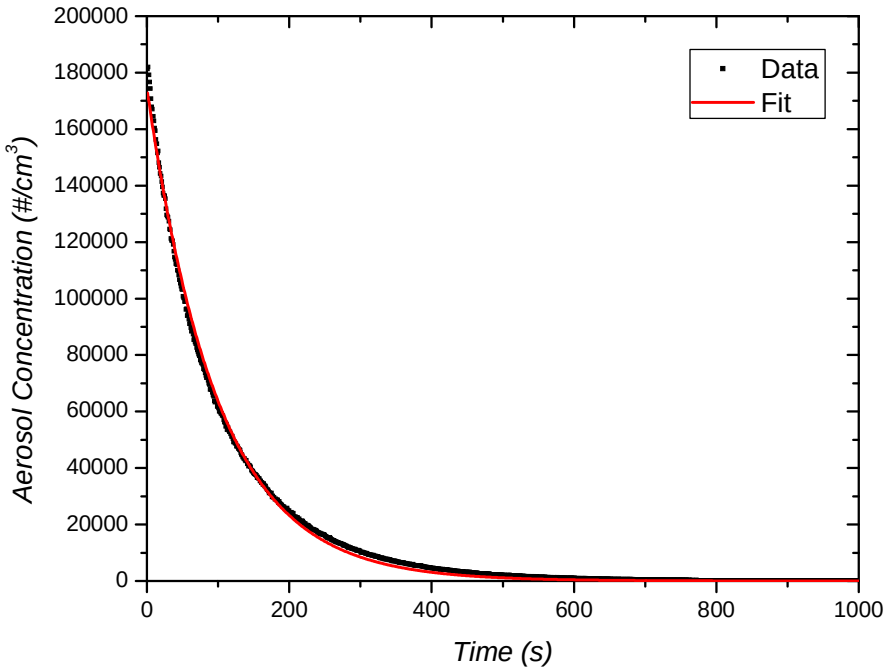

Figure 26. Aerosol concentration decay in closed aerosol system.

4. CONCLUSIONS AND FUTURE WORK

Two cavity enhanced spectroscopy based sensors have been developed for measurement of aerosols and hydrogen chloride with the ultimate goal of improving the understanding of the earth's energy balance. This thesis has described the operation and validation of an HCl sensor utilizing continuous-wave cavity ring-down spectroscopy. Relatively low-cost NIR components, similar to those used in telecommunications, were used to create the instrument. The instrument features HCl detection limits of single-digit pptv with optimum integration times of ~30 s and measurement settling times of ~4 minutes. Calibration studies have shown good agreement with expected values (better than ~10%), and the instrument was also demonstrated in a field campaign, showing consistency against other HCl instruments. The operation of an aerosol extinction sensor utilizing cavity enhanced absorption spectroscopy has also been described. A custom supercontinuum light source was directed into an external cavity comprised of broadband prism retroreflectors, the output signal of which was detected and converted into extinction coefficient. The instrument features a minimum detectable extinction coefficient of 8×10^{-8} cm^{-1} for 10 ms collection time. In the remainder of this section, possible improvements are discussed.

4.1 HYDROGEN CHLORIDE CRDS IMPROVEMENTS

From an optical point of view, several improvements could be considered for the cavity photodetector. First, a detector and amplifier combination with somewhat lower bandwidth (of ~400 kHz) would allow faithful measurement of the ring-down signal while lowering the adverse effects of high-frequency noise. Second, a thermo-electrically cooled photodiode could be used

to reduce the detector dark noise. Further, improved sensitivity can be obtained from more complicated CRDS schemes, though at the cost of increased hardware cost and complexity. One such example is to use a Pound-Drever-Hall locked cavity similar to Paldus et al. (ref Spence, 2000) where the laser and cavity frequencies are locked together such that higher ring-down acquisition rates of several kHz are possible. It would be reasonable to expect a factor of ~5 or more improvement in detection sensitivity by implementing this technique into the presented instrument.

From a packaging point of view, a more compact and robust design would be attractive for studies on aircraft or boats. The overall dimensions of the CRDS instrument are ~1.4×1.2×0.55 m. Currently, a commercial optical breadboard is used to mount all of the optical components while a straightforward improvement would be to use a smaller dedicated breadboard that could be mounted on a spring-damping system for improved vibration isolation. Further, the data acquisition computer uses a relatively large PCI DAQ card (PCI-6132) which could be replaced with a smaller and faster PCIe card. Issues related to the sticky gas adsorption can also be further investigated, with the goal of reducing the settling time, such as possible sample line passivation procedures [24].

Finally, as can be seen in Fig. 2, the current system can readily detect nearby spectral absorption lines due to water and methane. While these lines are not optimum selections for these molecules, they could be detected concurrently with HCl with detection limits of ~5 ppmv and ~2 ppbv for water and methane respectively (based on scaling the HCl data by relative linestrengths). Additionally, by changing only the laser, cavity mirrors, and quarter-wave plate, other NIR absorbing molecules such as CO, CO_2, and H_2S would be readily measurable.

4.2 AEROSOL CEAS IMPROVEMENTS

A number of improvements can be made to the CEAS aerosol sensor. For the sake of organization, these improvements can be divided into the aerosol delivery system and optical setup.

4.2.1 AEROSOL DELIVERY SYSTEM

As explained earlier, the closed aerosol test apparatus (discussed in 3.3) was developed after the "proof-of-concept" phase and, therefore, has not undergone a complete characterization. For future work, more effort must be put towards understanding the flow dynamics inside the aerosol chamber in order to comprehend aerosol concentration distribution. For example, it is assumed that the concentration across the laser sensing region is constant; however, large losses due to the acrylic exoskeleton or pressure variability in the dilution/vacuum flow subsystems could be creating a variable concentration (non-zero gradient). On a similar note, the CPC could be selectively probing near the laser sensing region and misrepresenting results. Finally, extensive leak testing is necessary in order to verify that aerosol is not unintentionally leaking out or ambient air is leaking in. Next, the effects of this aerosol apparatus on the pre-existing optical setup must be studied in greater depth. As expressed in 3.3, the retaining plate that mounts the optical window to the test apparatus induces birefringence and hence, decreases instrument sensitivity. Even though comparable sensitivity has been achieved with the closed versus open aerosol delivery system, understanding this birefringence is crucial in designing future instruments. Furthermore, investigating the role of acrylic thermal expansion on window birefringence could yield beneficial results. Finally and most importantly, the aerosol flow

system and CEAS sensor must be validated. In order to validate and calibrate this instrument, the ammonium sulfate could be introduced into the aerosol system. Since ammonium sulfate has no imaginary index of refraction (i.e. no absorption), extinction and scatter coefficient are equivalent. Hence, a multiple wavelength nephelometer (to measure scatter coefficient) can be run in parallel with the CEAS instrument for sensor verification.

Characterizing the current closed aerosol apparatus not only benefits aerosol measurement accuracy but also would aid in designing a more streamlined instrument. Since a preliminary characterization of the current setup has been completed, presented here are suggestions for future improvements. First, an improved test apparatus would benefit from being constructed out of steel in order to alleviate any concentration distribution issues related to static charge of the acrylic. Also, the steel would allow for better sealing since o-ring groove can be much more easily machined in steel than acrylic. Steel would add extra structural support; the only drawback to using this material is cost and fabrication difficulty. Second, it would be beneficial to decrease the size of the overall chamber in order to decrease residence time. As described in 3.3.2, the $1/e$ time constant is 100 s which is significantly long for a field instrument. It is important to note that a larger aerosol flow rate would decrease residence time, however with atomizers, this flow rate is fixed. Finally, this aerosol apparatus would benefit from an optical rearrangement. Rather than trying to reduce stress on the optical window, the polarizer could be placed downstream (i.e. inside the test chamber) of the window. This arrangement would alleviate birefringence related problems with the window; the only issue is the polarizer would need to be purged.

Once the current flow system has been methodically analyzed and/or replaced with the next iteration design, the instrument can theoretically measure extinction coefficient with the following aerosol setup (Figure 27).

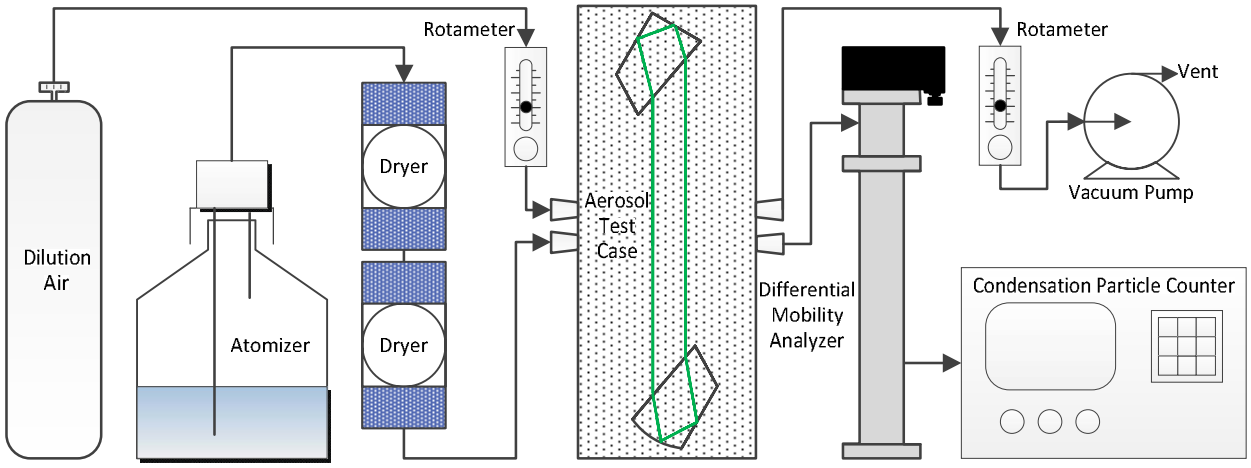

Figure 27 - Closed delivery system for aerosol generation.

The atomizer (or nebulizer) creates a polydisperse aerosol distribution which is dried and introduced into the closed aerosol test apparatus. A bottle of dilution air controlled by a rotameter allows the user to vary aerosol concentration. The CEAS sensor outputs the time averaged signal which can be converted to extinction coefficient. Meanwhile, a sample near the laser sensing region is pulled into a Differential Mobility Analyzer (DMA) used in conjunction with a Condensation Particle Counter (CPC) to measure concentration as a function of aerosol diameter. Using an algorithm, the measured extinction coefficient for the polydisperse aerosol can be converted into extinction coefficient as a function of diameter. With the data gathered from this sensor (ideally in combination with a photoacoustic spectrometer, e.g. as is currently being developed by collaborator Dr. Kevin Lehmann), various aerosol optical properties (e.g. SSA, indices of refraction, etc.) can be determined and used to update radiative forcing models.

4.2.2 OPTICAL SETUP

For a future system, sensitivity could be theoretically improved by a factor of ~8 to reach the level of 10^{-9} cm^{-1} $Hz^{-1/2}$ (0.1 Mm in 1-s), which could be achieved with the combination of a brighter light source and improved system configuration. The current experiments have used a custom laser pumped supercontinuum fiber having spectral power of approximately 0.11 mW/nm (from fiber output of ~200 mW, after excluding ~100 mW of residual 1064 nm pump light, spread over approximately 1800 nm from 500 nm to 2300 nm). As an alternative, a commercial supercontinuum source could be used (further described below) having (average) spectral brightness of ~1.5 mW/nm. Thus, the new source would provide approximately 14 times more spectral power which would improve the sensitivity by a factor of ~4 based on shot-noise (square-root scaling). Achieving the needed improvement (factor of ~8) would thus require an additional improvement of a factor of 2 which should be readily available by improving the mode-matching and alignment (to obtain higher effective reflectivity) and/or improving the monochromator and CCD detection (optimizing slit width, grating, and input f#).

The above discussion suggests that a final extinction coefficient sensitivity of ~$1x10^{-9}$ cm^{-1} $Hz^{-1/2}$ or equivalently 0.1 Mm^{-1} $Hz^{-1/2}$ can be reasonably attained. Moosmüller *et al* [100] state that an extinction coefficient sensitivity of 1 Mm^{-1} is needed for atmospheric aerosol detection based on comparison with Rayleigh scattering. Thus, a detection limits in extinction coefficient of ~$1x10^{-9}$ cm^{-1} (0.1 Mm^{-1}) can be achieved in one second, i.e. ten times the needed sensitivity for atmospheric measurements, based upon straightforward scaling of previously published results. Clearly, this level and time response is desirable for future field instruments including use on airplanes where the resulting spatial resolution will be about 150 m (based on

typical flight speed of 150 m/s). The sensitivity also compares favorably with those of current laboratory CRDS systems (even though the latter operate at only a single, or few, wavelengths), for example, Lang-Yona *et al*. achieve 1.5×10^{-9} cm^{-1} $Hz^{-1/2}$ (6.7×10^{-10} cm^{-1} in 5 seconds) with an instrument operating at a single-wavelength [36]. Based upon the experience with the existing system, an accuracy of a few percent and a very large dynamic range (at least 1000:1) is anticipated for the aerosol detection instrument. (Achieving accuracy of less than several percent is straightforward with CRDS aerosol measurements, e.g., Lang-Yona *et al*. [101] report an accuracy of 2% in measured extinction cross-sections of polystyrene latex calibration particles.) The base system, with these specifications, will operate with a wavelength range of 500-975 nm over which the supercontinuum output and CCD quantum efficiency are relatively flat.

Owing to the importance of aerosol optical measurements at shorter wavelengths, especially for brown-carbon aerosols, future work should also extend from the current limit of 500 nm to a lower limit, as is further discussed below.

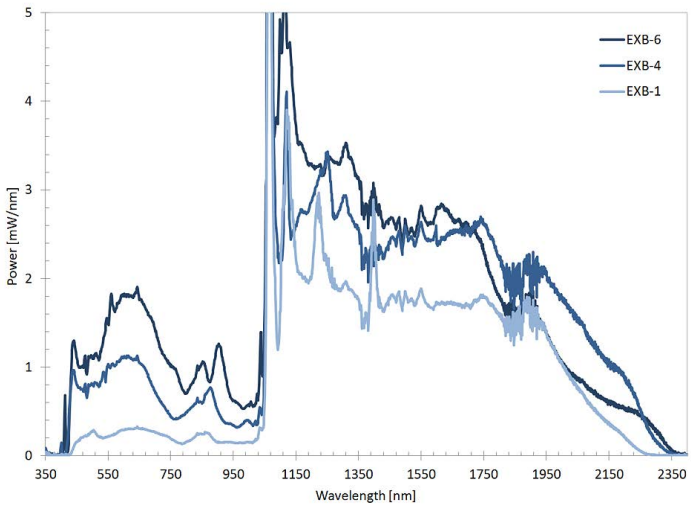

Figure 28 - Power spectra of supercontinuum output from commercial sources from NKT Photonics planned for Phase II.

The system described in 3.1 is fairly typical for “standard” supercontinuum fiber pumping with intensity rapidly dropping below ~480-500 nm. While there has been some academic work on shorter wavelength generation by fiber pumping [102], [103], future work could capitalize on recent improvements in commercial fiber pumped SC systems that allow high-brightness and improved short-wavelength coverage. Specifically, the Blue EXB-6 supercontinuum source from NKT Photonics could be used [104]. This source is also based on fiber pumped supercontinuum but uses a MHz repetition rate picosecond laser, along with an optimized fiber and pump conditions to achieve high spectral power and a short wavelength edge of ~400 nm, as shown in Figure 28. Although research has been conducted on CaF2 prisms for ultraviolet operation [81], SiO_2 prisms would be sufficient to reach 400 nm and also allow for instrument simplicity.

REFERENCES

[1] IPCC, S. Solomon, M. Qin, M. Manning, Z. Chen, M. Marquis, K. B. Averyt, M. Tignor, and H. L. Miller, *Contribution of Working Group I to the Fourth Assessment Report of the Intergovernmental Panel on Climate Change, 2007*. 2007, pp. 1–1007.

[2] V. Ramaswamy, O. Boucher, J. Haigh, D. Hauglustaine, J. Haywood, G. Myhre, T. Nakajima, G. Y. Shi, S. Solomon, R. Betts, R. Charlson, C. Chuang, J. S. Daniel, A. Del Genio, R. Van Dorland, J. Feichter, J. Fuglestvedt, P. M. De F Forster, S. J. Ghan, A. Jones, J. T. Kiehl, D. Koch, C. Land, J. Lean, U. Lohmann, K. Minschwaner, J. E. Penner, D. L. Roberts, H. Rodhe, G. J. Roelofs, L. D. Rotstayn, T. L. Schneider, U. Schumann, S. E. Schwartz, M. D. Schwarzkopf, K. P. Shine, S. Smith, D. S. Stevenson, F. Stordal, I. Tegen, and Y. Zhang, "Radiative Forcing of Climate Change: Climate Change 2001: Working Group I: The Scientific Basis." pp. 349–416, 2001.

[3] J. Haywood and O. Boucher, "Estimates of the direct and indirect radiative forcing due to tropospheric aerosols: A review," *Reviews of Geophysics*, vol. 38, no. 4, pp. 513–543, 2000.

[4] R. J. Charlson, S. E. Schwartz, J. M. Hales, R. D. Cess, J. A. Coakley, and D. J. Hofmann, "Climate Forcing by Anthropogenic Aerosols," *Science*, vol. 255, no. 5043, pp. 423–430, 1992.

[5] Pacific Northwest National Laboratory, "Aerosol Formation, Aging, and Transport." [Online]. Available: http://www.pnnl.gov/atmospheric/research/aci/aci_aerosol_formation.stm. [Accessed: 05-Jul-2012].

[6] J. E. Penner, M. Andreae, H. Annegarn, L. Barrie, J. Feichter, D. Hegg, A. Jayaraman, R. Leaitch, D. Murphy, J. Nganga, P. G., A. Ackerman, P. Adams, P. Austin, R. Boers, O. Boucher, M. Chin, C. Chuang, B. Collins, W. Cooke, P. Demott, Y. Feng, H. Fischer, I. Fung, S. Ghan, P. Ginoux, S. Gong, A. Guenther, M. Herzog, A. Higurashi, Y. Kaufman, A. Kettle, J. Kiehl, D. Koch, G. Lammel, C. Land, U. Lohmann, S. Madronich, E. Mancini, M. Mishchenko, T. Nakajima, P. Quinn, P. Rasch, D. L. Roberts, D. Savoie, S. Schwartz, J. Seinfeld, B. Soden, D. Tanré, K. Taylor, I. Tegen, X. Tie, G. Vali, R. Van Dingenen, and M. Van Weele, "Aerosols, their Direct and Indirect Effects: Climate Change 2001: Working Group I: The Scientific Basis," 2001, pp. 290–348.

[7] M. D. King, Y. J. Kaufman, D. Tanre, and T. Nakajima, "Remote Sensing of Tropospheric Aerosols from Space: Past, Present, and Future," *Bulletin of the American Meterological Society*, pp. 2229–2259, 1999.

[8] R. Vogt, P. J. Crutzen, and R. Sander, "A mechanism for halogen release from sea-salt aerosol in the remote marine boundary layer," *Nature*, vol. 383, pp. 327–329, 1996.

[9] W. R. Simpson, R. von Glasow, K. Riedel, P. Anderson, P. Ariya, J. Bottenheim, J. Burrows, L. Carpenter, U. Frieß, M. E. Goodsite, D. Heard, M. Hutterli, H.-W. Jacobi, L. Kaleschke, B. Neff, J. Plane, U. Platt, A. Richter, H. Roscoe, R. Sander, P. Shepson, J. Sodeau, A. Steffen, T. Wagner, and E. Wolff, "Halogens and their role in polar boundary-layer ozone depletion," *Atmospheric Chemistry and Physics Discussions*, vol. 7, pp. 4285–4403, Mar. 2007.

[10] P. L. Tanaka, S. Oldfield, J. D. Neece, C. B. Mullins, and D. T. Allen, "Anthropogenic Sources of Chlorine and Ozone Formation in Urban Atmospheres," *Environmental Science & Technology*, vol. 34, no. 21, pp. 4470–4473, Nov. 2000.

[11] E. M. Knipping and D. Dabdub, "Impact of chlorine emissions from sea-salt aerosol on coastal urban ozone.," *Environmental science & technology*, vol. 37, no. 2, pp. 275–84, Jan. 2003.

[12] U. Platt, W. Allan, and D. Lowe, "Hemispheric average Cl atom concentration from 13 C / 12 C ratios in atmospheric methane," *Atmospheric Chemistry and Physics*, vol. 4, pp. 2393–2399, 2004.

[13] W. Allan, H. Struthers, and D. C. Lowe, "Methane carbon isotope effects caused by atomic chlorine in the marine boundary layer: Global model results compared with Southern Hemisphere measurements," *Journal of Geophysical Research*, vol. 112, no. D04306, pp. 1–10, Feb. 2007.

[14] B. T. Jobson, H. Niki, Y. Yokouchi, J. Bottenheim, F. Hopper, and R. Leaitch, "Measurements of C2-C6 hydrocarbons during the Polar Sunrise 1992 Experiment: Evidence for Cl atom and Br atom chemistry," *Journal of Geophysical Research*, vol. 99, no. D12, pp. 25355–25368, 1994.

[15] V. Achard, M. De Mazibre, C. Camy-Peyret, F. Karcher, and C. Lippens, "Spaceborne measurements of the upper stratospheric HCL vertical distribution in early 1992 and the trend in total stratospheric," *Journal of Geophysical Research*, vol. 102, no. D7, pp. 8985–8990, 1997.

[16] T. E. Graedel and W. C. Keene, "Tropospheric budget of reactive chlorine The nine species , to be HOCI and / or vigorous chlorine cycling appears to occur among seasalt aerosol , and CId . The principal of the annual stratospheric chlorine," *Global Biogeochem. Cycles*, vol. 9, no. 1, pp. 47–77, 1995.

[17] W. C. Keene, M. A. K. Khalil, D. . . Erickson, A. Mcculloch, T. E. Graedel, J. M. Lobert, M. L. Aucott, S. L. Gong, B. Harper, G. Kleiman, P. Midgley, R. M. Moore, W. T. Sturges, C. M. Benkovitz, V. Koropalov, L. A. Barrie, and Y. F. Li, "Composite global emissions of reactive chlorine from anthropogenic and natural sources : Reactive Chlorine Emissions Inventory," *Journal of Geophysical Research*, vol. 104, no. D7, pp. 8429–8440, 1999.

[18] W. C. Keene, J. Stutz, A. A. P. Pszenny, J. R. Maben, E. V. Fischer, A. M. Smith, R. von Glasow, S. Pechtl, B. C. Sive, and R. K. Varner, "Inorganic chlorine and bromine in coastal New England air during summer," *Journal of Geophysical Research*, vol. 112, no. D10S12, pp. 1–15, May 2007.

[19] A. A. P. Pszenny, J. Moldanov, W. C. Keene, R. Sander, J. R. Maben, M. Martinez, P. J. Crutzen, D. Perner, and R. G. Prinn., "Halogen cycling and aerosol pH in the Hawaiian marine boundary layer," *Atmospheric Chemistry and Physics*, vol. 4, pp. 147–168, 2004.

[20] S. Kim, L. G. Huey, R. E. Stickel, R. B. Pierce, G. Chen, M. a. Avery, J. E. Dibb, G. S. Diskin, G. W. Sachse, C. S. McNaughton, a. D. Clarke, B. E. Anderson, and D. R. Blake, "Airborne measurements of HCl from the marine boundary layer to the lower stratosphere over the North Pacific Ocean during INTEX-B," *Atmospheric Chemistry and Physics Discussions*, vol. 8, pp. 3563–3595, Feb. 2008.

[21] J. R. Maben, W. C. Keene, A. A. P. Pszenny, and J. N. Galloway, "Volatile inorganic Cl in surface air over eastern North America," *Geophysical Research Letters*, vol. 22, no. 24, pp. 3513–3516, Dec. 1995.

[22] P. Ortwein, W. Woiwode, S. Wagner, M. Gisi, and V. Ebert, "Laser-based measurements of line strength, self- and pressure-broadening coefficients of the H35Cl R(3) absorption line in the first overtone region for pressures up to 1 MPa," *Applied Physics B*, vol. 100, pp. 341–347, 2010.

[23] O. Bjoroey, K. H. Haugholt, and T. Jaeger, "Diode laser spectroscopy of gaseous HC1," *Quantum Electronics*, vol. 26, no. 12, pp. 1090–1092, 1996.

[24] W. C. Keene, J. R. Maben, A. A. P. Pszenny, and J. N. Galloway, "Measurement Technique for Inorganic Chlorine Gases in the Marine Boundary Layer," *Eviron. Sci. Technol.*, vol. 27, no. 5, pp. 866–874, 1993.

[25] E. Scheuer, R. W. Talbot, J. E. Dibb, G. K. Seid, and D. L., "Seasonal distributions of fine aerosol sulfate in the North American Arctic basin during TOPSE," *Journal of Geophysical Research*, vol. 108, no. D4, p. 8370, 2003.

[26] J. M. Roberts, P. Veres, C. Warneke, J. A. Neuman, R. A. Washenfelder, S. S. Brown, M. Baasandorj, J. B. Burkholder, I. R. Burling, T. J. Johnson, R. J. Yokelson, and J. de Gouw, "Measurement of HONO, HNCO, and other inorganic acids by negative-ion proton-transfer chemical-ionization mass spectrometry (NI-PT-CIMS): application to biomass burning emissions," *Atmospheric Measurement Techniques Discussions*, vol. 3, pp. 301–331, Jan. 2010.

[27] T. C. VandenBoer, N. Wagner, C. J. Young, B. Dube, T. P. Riedel, R. Bahreini, F. Oz, turk, C. Warneke, J. A. De Gouw, W. C. Keene, A. Pszenny, T. J.A., D. E. Wol fe, S. S. Brown, A. M. Middlebrook, and J. M. Roberts, "Vertical profiles of HONO during

NACHTT 2011: Relative importance of heterogeneous production on aerosol versus the ground surface," *AGU Fall Meeting Abstracts*, p. F421, 2011.

[28] T. C. VandenBoer, M. Z. Markovic, and P. Veres, "HCl surface measurements during CalNex and vertical profiles during NACHTT: Implications of partitioning thermodynamics, acid displacement and chlorine activation through heterogeneous chemistry," in *242nd National Meeting of the American-Chemical-Society (ACS)*, 2011.

[29] T. P. Marcy, D. W. Fahey, R. S. Gao, P. J. Popp, E. C. Richard, T. L. Thompson, K. H. Rosenlof, E. A. Ray, R. J. Salawitch, C. S. Atherton, D. J. Bergmann, B. A. Ridley, A. J. Weinheimer, M. Loewenstein, E. M. Weinstock, and M. J. Mahoney, "Quantifying stratospheric ozone in the upper troposphere with in situ measurements of HCl.," *Science (New York, N.Y.)*, vol. 304, no. 5668, pp. 261–5, Apr. 2004.

[30] C. R. Webster, R. D. May, C. A. Trimble, R. G. Chave, and J. Kendall, "Aircraft (ER-2) laser infrared absorption spectrometer (ALIAS) for in-situ stratospheric measurements of HCl, N20, CH4, NO2, and HNO3," *Apllied Optics*, vol. 33, no. 3, pp. 454–472, 1994.

[31] D. C. Scott, R. L. Herman, C. R. Webster, R. D. May, G. J. Flesch, and E. J. Moyer, "Airborne laser infrared absorption spectrometer (ALIAS-II) for in situ atmospheric measurements of N2O, CH4, CO, HCl, and NO2 from balloon or remotely piloted aircraft platforms.," *Applied optics*, vol. 38, no. 21, pp. 4609–22, Jul. 1999.

[32] W. C. Hinds, *Aerosol Technology*, 2nd ed. Hoboken: John Wiley & Sons, Inc., 1999, pp. 349–378.

[33] V. Bulatov, Y. Chen, A. Khalmanov, and I. Schechter, "Absorption and scattering characterization of airborne microparticulates by a cavity ringdown technique.," *Analytical and bioanalytical chemistry*, vol. 384, pp. 155–60, Jan. 2006.

[34] E. Montilla, S. Mogo, V. Cachorro, J. Lopez, and a. de Frutos, "Absorption, scattering and single scattering albedo of aerosols obtained from in situ measurements in the subarctic coastal region of Norway," *Atmospheric Chemistry and Physics Discussions*, vol. 11, no. 1, pp. 2161–2182, Jan. 2011.

[35] J. Hansen, M. Sato, and R. Ruedy, "Radiative forcing and climate response," *Journal of Geophysical Research*, vol. 102, no. D6, pp. 6831–6864, 1997.

[36] H. C. Hulst, *Light scattering by small particles*, 2nd ed., vol. 48, no. 2. Mineola: John Wiley & Sons, 1981, pp. 1–245.

[37] C. F. Bohren, "Multiple scattering of light and some of its observable consequences," *Am. J. Phys.*, vol. 55, no. 6, pp. 524–533, 1986.

[38] J. D. Smith and D. B. Atkinson, “A portable pulsed cavity ring-down transmissometer for measurement of the optical extinction of the atmospheric aerosol,” *The Analyst*, vol. 126, no. 8, pp. 1216–1220, 2001.

[39] H. Moosmuller, W. P. Arnott, C. F. Rogers, J. C. Chow, and C. A. Frazier, “Photoacoustic and filter measurements related to aerosol light absorption during the Northern Front Range Air Quality Study (Colorado 1996/1997),” *Journal of Geophysical Research*, vol. 103, no. D21, pp. 28149–28157, 1998.

[40] S. Reid, V. Hobbs, J. Vanderlei, E. Weiss, and F. Eck, “Comparison of techniques for measuring shortwave absorption and black carbon content of aerosols from biomass burning in Brazil,” *Journal of Geophysical Research*, vol. 103, no. D24, pp. 31–32, 1998.

[41] Y. J. Kaufman, D. Tanrc, H. R. Gordon, T. Nakajima, J. Lenoble, R. Frouins, H. Grassl, B. M. Herman, M. D. King, and P. M. Teillet, “Passive remote sensing of tropospheric correction for the aerosol effect aerosol and atmospheric,” *Journal of Geophysical Research*, vol. 102, no. D14, pp. 16815–16830, 1997.

[42] R. Fraser and Y. Kaufman, “The Relative Importance of Aerosol Scattering and Absorption in Remote Sensing,” *IEEE Transaction of Geoscience and Remote Sensing*, vol. GE-23, no. 5, pp. 625–633, Sep. 1985.

[43] T. Nakajima and A. Higurashi, “AVHRR remote sensing of aerosol optical properties in the Persian Gulf region, summer 1991,” *Journal of Geophysical Research*, vol. 102, no. D14, pp. 16935–16946, 1997.

[44] K. W. Busch and M. A. Busch, “Cavity-Ringdown Spectroscopy,” *ACS Symposium Series*, vol. 720, pp. 1–7, 1999.

[45] G. Berden, R. Peeters, and G. Meijer, “Cavity ring-down spectroscopy : Experimental schemes and applications,” *Int. Reviews in Physical Chemistry*, vol. 4, pp. 565–607, 2000.

[46] R. Engeln, G. Berden, R. Peeters, and G. Meijer, “Cavity enhanced absorption and cavity enhanced magnetic rotation spectroscopy,” *Review of Scientific Instruments*, vol. 69, no. 11, pp. 3763–3769, 1998.

[47] A. O. Keefe, “Integrated cavity output analysis of ultra-weak absorption,” *Chemical Physics Letters*, pp. 331–336, 1998.

[48] S. S. Brown, “Absorption spectroscopy in high-finesse cavities for atmospheric studies.,” *Chemical reviews*, vol. 103, no. 12, pp. 5219–38, Dec. 2003.

[49] R. Wada, J. M. Beames, and A. J. Orr-ewing, “Measurement of IO radical concentrations in the marine boundary layer using a cavity ring-down spectrometer,” *J Atmos Chem*, vol. 58, pp. 69–87, 2007.

[50] A. W. Liu, S. Kassi, P. Malara, D. Romanini, V. I. Perevalov, S. A. Tashkun, S. M. Hu, and A. Campargue, "High sensitivity CW-cavity ring down spectroscopy of N2O near 1.5 μm (I) - Liu, A.W. et al..pdf," *Journal of molecular spectroscopy*, vol. 244, pp. 33–47, 2007.

[51] W. P. Dubé, S. S. Brown, H. D. Osthoff, M. R. Nunley, S. J. Ciciora, M. W. Paris, R. J. McLaughlin, and A. R. Ravishankara, "Aircraft instrument for simultaneous, in situ measurement of NO[sub 3] and N[sub 2]O[sub 5] via pulsed cavity ring-down spectroscopy," *Review of Scientific Instruments*, vol. 77, p. 034101, 2006.

[52] D. S. Venables, T. Gherman, J. Orphal, J. Wenger, and A. A. Ruth, "High Sensitivity in Situ Monitoring Simulation Chamber Using Incoherent Broadband Spectroscopy," *Environ. Sci. Technol.*, vol. 40, no. 21, pp. 6758–6763, 2006.

[53] A. Abo Riziq, C. Erlick, E. Dinar, and Y. Rudich, "Optical properties of absorbing and non-absorbing aerosols retrieved by cavity ring down (CRD) spectroscopy," *Atmospheric Chemistry and Physics*, vol. 7, pp. 1523–1536, Mar. 2007.

[54] C. Spindler, A. Abo Riziq, and Y. Rudich, "Retrieval of Aerosol Complex Refractive Index by Combining Cavity Ring Down Aerosol Spectrometer Measurements with Full Size Distribution Information," *Aerosol Science and Technology*, vol. 41, no. 11, pp. 1011–1017, Oct. 2007.

[55] T. Baynard, E. R. Lovejoy, A. Pettersson, S. S. Brown, D. Lack, H. Osthoff, P. Massoli, S. Ciciora, W. P. Dube, and A. R. Ravishankara, "Design and Application of a Pulsed Cavity Ring-Down Aerosol Extinction Spectrometer for Field Measurements," *Aerosol Science and Technology*, vol. 41, no. 4, pp. 447–462, Mar. 2007.

[56] V. Bulatov, M. Fisher, and I. Schechter, "Aerosol analysis by cavity-ring-down laser spectroscopy," vol. 466, pp. 1–9, 2002.

[57] T. J. A. Butler, J. L. Miller, and A. J. Orr-Ewing, "Cavity ring-down spectroscopy measurements of single aerosol particle extinction. I. The effect of position of a particle within the laser beam on extinction.," *The Journal of chemical physics*, vol. 126, no. 17, pp. 1–8, May 2007.

[58] A. G. Hallar, A. W. Strawa, B. Schmid, E. Andrews, J. Ogren, P. Sheridan, R. Ferrare, D. Covert, R. Elleman, H. Jonsson, K. Bokarius, and A. Luu, "Atmospheric Radiation Measurements Aerosol Intensive Operating Period: Comparison of aerosol scattering during coordinated flights," *Journal of Geophysical Research*, vol. 111, no. D05S09, pp. 1–17, 2006.

[59] C. R. Howie, C. J. Homer, R. J. Hopkins, and J. P. Reid, "Probing the evaporation of ternary ethanol-methanol-water droplets by cavity enhanced Raman scattering.," *Physical chemistry chemical physics*, vol. 9, pp. 5344–52, Oct. 2007.

[60] J. L. Miller and A. J. Orr-Ewing, “Cavity ring-down spectroscopy measurement of single aerosol particle extinction. II. Extinction of light by an aerosol particle in an optical cavity excited by a cw laser.,” *The Journal of chemical physics*, vol. 126, no. 174303, pp. 1–8, May 2007.

[61] H. Moosmüller, R. Varma, and W. P. Arnott, “Cavity Ring-Down and Cavity-Enhanced Detection Techniques for the Measurement of Aerosol Extinction,” *Aerosol Science and Technology*, vol. 39, no. 1, pp. 30–39, Jan. 2005.

[62] A. Pettersson, E. R. Lovejoy, C. A. Brock, S. S. Brown, and A. R. Ravishankara, “Measurement of aerosol optical extinction at 532 nm with pulsed cavity ring down spectroscopy,” *J. Aerosol Sci.*, vol. 35, pp. 995–1011, 2004.

[63] B. Richman, A. Kachanov, B. Paldus, and A. Strawa, “Novel detection of aerosols: combined cavity ring-down and fluorescence spectroscopy.,” *Optics express*, vol. 13, no. 9, pp. 3376–87, May 2005.

[64] A. Abo Riziq, M. Trainic, C. Erlick, E. Segre, and Y. Rudich, “Extinction efficiencies of coated absorbing aerosols measured by cavity ring down aerosol spectrometry,” *Atmospheric Chemistry and Physics*, vol. 8, pp. 1823–1833, Mar. 2008.

[65] S. Rudić, R. E. H. Miles, A. J. Orr-Ewing, and J. P. Reid, “Optical properties of micrometer size water droplets studied by cavity ringdown spectroscopy.,” *Applied optics*, vol. 46, no. 24, pp. 6142–50, Aug. 2007.

[66] A. W. Strawa and R. Castaneda, “The Measurement of Aerosol Optical Properties Using Continuous Wave Cavity Ring-Down Techniques,” *Journal of Atmospheric and Oceanic Technology*, vol. 20, pp. 454–465, 2003.

[67] A. W. Strawa, R. Elleman, A. G. Hallar, D. Covert, K. Ricci, R. Provencal, T. W. Owano, H. H. Jonsson, B. Schmid, A. P. Luu, K. Bokarius, and E. Andrews, “Comparison of in situ aerosol extinction and scattering coefficient measurements made during the Aerosol Intensive Operating Period,” *Journal of Geophysical Research*, vol. 111, no. D05S03, pp. 1–17, 2006.

[68] J. E. Thompson, N. Barta, D. Policarpio, and R. Duvall, “A fixed frequency aerosol albedometer.,” *Optics express*, vol. 16, no. 3, pp. 2191–205, Feb. 2008.

[69] J. M. Langridge, M. S. Richardson, D. Lack, D. Law, and D. M. Murphy, “Aircraft Instrument for Comprehensive Characterization of Aerosol Optical Properties, Part I: Wavelength-Dependent Optical Extinction and Its Relative Humidity Dependence Measured Using Cavity Ringdown Spectroscopy,” *Aerosol Science and Technology*, vol. 45, no. 11, pp. 1305–1318, Nov. 2011.

[70] R. Engeln, E. van den Berg, G. Meijer, L. Lin, G. M. H. Knippels, and A. F. G. van der Meer, "Cavity ring down spectroscopy with a free-electron laser," *Chemical Physics Letters*, vol. 269, pp. 293–297, 1997.

[71] J. J. Scherer, J. B. Paul, H. Jiao, and A. O'Keefe, "Broadband ringdown spectral photography.," *Applied optics*, vol. 40, no. 36, pp. 6725–32, Dec. 2001.

[72] V. L. Kasyutich, C. E. Canosa-Mas, C. Pfrang, S. Vaughan, and R. P. Wayne, "Off-axis continuous-wave cavity-enhanced absorption spectroscopy of narrow-band and broadband absorbers using red diode lasers," *Applied Physics B: Lasers and Optics*, vol. 75, pp. 755–761, Nov. 2002.

[73] S. M. Ball, J. M. Langridge, and R. L. Jones, "Broadband cavity enhanced absorption spectroscopy using light emitting diodes," *Chemical Physics Letters*, vol. 398, no. 1–3, pp. 68–74, Nov. 2004.

[74] M. J. Thorpe, K. D. Moll, R. J. Jones, B. Safdi, and J. Ye, "Broadband cavity ringdown spectroscopy for sensitive and rapid molecular detection.," *Science (New York, N.Y.)*, vol. 311, pp. 1595–9, Mar. 2006.

[75] S. E. Fiedler, G. Hoheisel, A. A. Ruth, and A. Hese, "Incoherent broad-band cavity-enhanced absorption spectroscopy of azulene in a supersonic jet," *Chemical Physics Letters*, vol. 382, no. 3–4, pp. 447–453, 2003.

[76] R. Engeln and G. Meijer, "A Fourier Transform Cavity Ring Down Spectrometer," *Rev. Sci. Instr.*, vol. 2708, pp. 1–7, 1996.

[77] A. A. Ruth, J. Orphal, and S. E. Fiedler, "Fourier-transform cavity-enhanced absorption spectroscopy using an incoherent broadband light source.," *Applied optics*, vol. 46, no. 17, pp. 3611–6, Jun. 2007.

[78] E. Hamers, D. Schram, and R. Engeln, "Fourier transform phase shift cavity ring down spectroscopy," *Chemical Physics Letters*, vol. 365, no. 3–4, pp. 237–243, 2002.

[79] K. K. Lehmann and P. Rabinowitz, "High-Finesse Optical Resonator for Cavity Ring-Down Spectroscopy based upon Brewster's Angle Prism Retroreflectors. - Lehmann, K.K. et al..pdf," 1999.

[80] P. Johnston and K. K. Lehmann, "Supercontinuum based broadband cavity enhanced absorption spectroscopy," in *62nd International Sympoium on Molecular Spectroscopy*, 2007.

[81] K. K. Lehmann, P. S. Johnston, and P. Rabinowitz, "Brewster angle prism retroreflectors for cavity enhanced spectroscopy.," *Applied optics*, vol. 48, no. 16, pp. 2966–78, Jun. 2009.

[82] P. S. Johnston and K. K. Lehmann, "Cavity enhanced absorption spectroscopy using a broadband prism cavity and a supercontinuum source.," *Optics express*, vol. 16, no. 19, pp. 15013–23, Sep. 2008.

[83] P. Russell, "Photonic crystal fibers.," *Science*, vol. 299, no. 5605, pp. 358–62, Jan. 2003.

[84] W. J. Wadsworth, A. Ortigosa-Blanch, J. C. Knight, T. A. Birks, T.-P. M. Man, and P. S. J. Russell, "Supercontinuum generation in photonic crystal fibers and optical fiber tapers: a novel light source," *Journal of the Optical Society of America B*, vol. 19, no. 9, p. 2148, Sep. 2002.

[85] J. M. Dudley and J. R. Taylor, "Ten years of nonlinear optics in photonic crystal fibre," *Nature Photonics*, vol. 3, pp. 85–90, Feb. 2009.

[86] W. Wadsworth, N. Joly, J. Knight, T. Birks, F. Biancalana, and P. Russell, "Supercontinuum and four-wave mixing with Q-switched pulses in endlessly single-mode photonic crystal fibres.," *Optics express*, vol. 12, no. 2, pp. 299–309, Jan. 2004.

[87] L. S. Rothman, I. E. Gordon, A. Barbe, D. C. Benner, P. F. Bernath, M. Birk, V. Boudon, L. R. Brown, A. Campargue, J.-P. Champion, K. Chance, L. H. Coudert, V. Dana, V. M. Devi, S. Fally, J.-M. Flaud, R. R. Gamache, A. Goldman, D. Jacquemart, I. Kleiner, N. Lacome, W. J. Lafferty, J.-Y. Mandin, S. T. Massie, S. N. Mikhailenko, C. E. Miller, N. Moazzen-Ahmadi, O. V. Naumenko, A. V. Nikitin, J. Orphal, V. I. Perevalov, A. Perrin, A. Predoi-Cross, C. P. Rinsland, M. Rotger, M. Šimečková, M. a. H. Smith, K. Sung, S. a. Tashkun, J. Tennyson, R. a. Toth, A. C. Vandaele, and J. Vander Auwera, "The HITRAN 2008 molecular spectroscopic database," *Journal of Quantitative Spectroscopy and Radiative Transfer*, vol. 110, no. 9–10, pp. 533–572, Jun. 2009.

[88] M. De Rosa, C. Nardini, C. Piccolo, C. Corsi, and F. D'Amato, "Pressure broadening and shift of transitions of the first overtone of HCl," *Applied Physics B*, vol. 72, pp. 245–248, Jan. 2001.

[89] P. Weibring, D. Richter, J. G. Walega, L. Rippe, and A. Fried, "Difference frequency generation spectrometer for simultaneous multispecies detection," *Opt. Express*, vol. 18, no. 26, pp. 27670–27681, Dec. 2010.

[90] R. H. Tipping, "Calculation of Spectroscopic Parameters for Diatomic Molecules of Atmospheric Interest," *PHYSICS, A. U. U. D. O., and ASTRONOMY*, 1990.

[91] H. Kogelnik and T. Li, "Laser Beams and Resonators," *Appl. Opt.*, vol. 5, no. 10, pp. 1550–1567, Oct. 1966.

[92] R. K. Hansen, E. Klingbeil, W. Mattison, D. Koch, E. Webber, and M. Seitzman, *Introduction to Spectroscopy and Laser Diagnostics for Gases*. Palo Alto: Stanford University, 2006, pp. 1–381.

[93] S. S. Brown, R. W. Wilson, and A. R. Ravishankara, “Absolute Intensities for Third and Fourth Overtone Absorptions in HNO3 and H2O2 Measured by Cavity Ring Down Spectroscopy,” *The Journal of Physical Chemistry A*, vol. 104, no. 21, pp. 4976–4983, 2000.

[94] B. A. Paldus and A. A. Kachanov, “An historical overview of cavity-enhanced methods,” *Can. J. Phys.*, vol. 83, no. 10, pp. 975–999, 2005.

[95] P. Zalicki and R. N. Zare, “Cavity ring-down spectroscopy for quantitative absorption measurements,” *Chem. Phys.*, vol. 102, no. 7, pp. 2708–2717, 1995.

[96] H. Huang and K. K. Lehmann, “Long-term stability in continuous wave cavity ringdown spectroscopy experiments.,” *Applied optics*, vol. 49, no. 8, pp. 1378–87, Mar. 2010.

[97] A. Fried, R. Sams, and W. W. Berg, “Application of tunable diode laser absorption for trace stratospheric measurements of HCl: laboratory results,” *Applied optics*, vol. 23, no. 11, p. 1867, Jun. 1984.

[98] A. Pszenny, W. C. Keene, R. Sander, R. Bearekman, B. Deegan, J. R. Maben, C. Warrick-Wriston, and A. Young, “Salt in the Air during the Nitrogen, Aerosol Composition, and Halogens on a Tall Tower (NACHTT) Campaign,” *AGU Fall Meeting Abstracts*, p. F418, 2011.

[99] J. B. Paul, L. Lapson, and J. G. Anderson, “Ultrasensitive absorption spectroscopy with a high-finesse optical cavity and off-axis alignment.,” *Applied optics*, vol. 40, no. 27, pp. 4904–10, Sep. 2001.

[100] H. Moosmuller, R. K. Chakrabarty, and W. P. Arnott, “Aerosol light absorption and its measurement A review,” *Journal of Quantitative Spectroscopy and Radiative Transfer*, vol. 110, pp. 844–878, 2009.

[101] N. Lang-Yona, Y. Rudich, E. Segre, E. Dinar, and A. Abo-Riziq, “Complex refractive indices of aerosols retrieved by continuous wave-cavity ring down aerosol spectrometer.,” *Analytical chemistry*, vol. 81, no. 5, pp. 1762–9, Mar. 2009.

[102] A. Kudlinski, A. K. George, and J. C. Knight, “Zero-dispersion wavelength decreasing photonic crystal fibers for ultraviolet-extended supercontinuum generation Abstract :,” *Opt. Express*, vol. 14, no. 12, pp. 5715–5722, 2006.

[103] R. J. Bartula, J. W. Walewski, and S. T. Sanders, “Generation of ultraviolet broadband light in a single-mode fiber,” *Appl. Phys. B*, vol. 84, pp. 395–400, 2006.

[104] NKT Photonics, “SuperK EXTREME: High Power Supercontinuum fiber laser series,” 2013. [Online]. Available: http://www.nktphotonics.com/superk_extreme_specifications.